



Full length article

Data-informed simulation of temperature effects in finite element models for structural health monitoring using inverse surrogate modeling

Soroosh Kamali ^a,* Rosario Ceravolo ^b, Alessandro Marzani ^a^a Department of Civil, Chemical, Environmental and Materials Engineering, University of Bologna, Bologna, Italy^b Department of Structural, Geotechnical and Building Engineering, Politecnico di Torino, Turin, Italy

ARTICLE INFO

Communicated by L. Mevel

Keywords:

Structural health monitoring
 Temperature modeling
 Inverse surrogate modeling
 FEM updating
 Damage detection
 Modal analysis

ABSTRACT

This work presents a data-informed framework to simulate temperature effects in a finite element model (FEM) for structural health monitoring (SHM), enabling realistic generation of synthetic modal data for both healthy and damaged states. A challenge in vibration-based SHM is that real damaged data are rarely available, so damage detection and classification methods are often validated using FEM simulations. However, temperature strongly affects modal data through changes in stiffness, connections, and boundary conditions, and these effects are difficult to reproduce realistically using standard thermo-mechanical assumptions, especially when only few temperature measurements are available. The proposed approach combines field monitoring data with an updated FEM through inverse surrogate modeling. First, an inverse surrogate model is trained on FEM simulations to recover temperature-sensitive mechanical parameters (e.g., Young's modulus of elasticity) from modal frequencies. Then, this surrogate is applied to long-term monitoring data to estimate how these parameters evolve with temperature. A second regression model then learns a direct mapping from temperature to FEM parameters. Injecting these temperature-dependent parameters into the FEM allows simulation of realistic temperature-frequency trends, for both healthy and damage scenarios. The method is demonstrated on a numerical truss and on the KW51 railway bridge. Results show high accuracy in modal frequency prediction and consistent anomaly detection performance, indicating that the framework reproduces in-situ thermal effects without requiring explicit thermo-mechanical modeling, while preserving damage detectability under temperature variations.

1. Introduction

Vibration-based structural health monitoring (SHM) is increasingly becoming an important discipline for evaluating the safety and health of the civil structures and infrastructures. By monitoring variations in modal properties, such as natural frequencies, SHM systems can detect damage or degradation before catastrophic failure occurs [1–6]. However, the effective validation of damage detection and classification algorithms remains constrained by a fundamental limitation: the scarcity of real damage data. In most long-term monitoring campaigns, structures operate under healthy conditions throughout the data collection period, and genuine damage events are either nonexistent or occur only after years of service. Consequently, it is not easy to construct large, labeled datasets encompassing both healthy and damage scenarios under realistic environmental and operational (EO) variability. This

* Corresponding author.

E-mail address: soroosh.kamali2@unibo.it (S. Kamali).<https://doi.org/10.1016/j.ymssp.2026.114519>

Received 23 December 2025; Received in revised form 17 April 2026; Accepted 27 May 2026

0888-3270/© 2026 The Authors. Published by Elsevier Ltd. This is an open access article under the CC BY license (<http://creativecommons.org/licenses/by/4.0/>).

data scarcity hinders the quantitative evaluation of damage indexes, the tuning of detection thresholds, and the estimation of the probability of detection (POD) in the presence of EO fluctuations such as temperature, humidity, or load changes [7–12].

To overcome this limitation, a common strategy is to generate synthetic datasets using finite element models (FEMs) [13–15]. A baseline FEM is first updated to reproduce the measured modal characteristics of the healthy structure, typically by minimizing the discrepancy between experimental and simulated modal frequencies [16]. Once the model is calibrated, it can be systematically used to generate various damage scenarios by reducing stiffness, changing connection properties, or modifying boundary conditions. The corresponding modal frequencies of these damage scenarios build a dataset that is then used to test SHM algorithms. Finally, to enhance realism, simulated data are often contaminated with stochastic noise derived from the statistical properties of the baseline measurements.

Despite the practical advantages of FEM-based data generation, one major challenge remains unresolved: the realistic modeling of temperature effects, particularly for damage scenarios. Temperature variations significantly influence the dynamic response of the structures by altering material stiffness, connection rigidity, and support boundary conditions. Seasonal and daily temperature cycles can induce modal frequency shifts which could be confused with damage, increasing the probability of false alarms (PFA) and reducing the POD. If temperature effects are not properly modeled in the synthetic data, the simulated modal responses will lack realism, and temperature compensation algorithms trained on baseline data cannot be meaningfully evaluated under damaged conditions [17]. Consequently, the reliability of any damage detection assessment using such synthetic datasets becomes limited.

To overcome this issue, previous studies have investigated temperature effects on structural responses through a variety of modeling and data-driven strategies, which can be grouped into three main categories: (A) empirical works that establish regression-based relationships between measured temperatures and monitoring data; (B) temperature compensation approaches that remove or normalize thermal effects prior to damage detection or model updating; and (C) finite element studies that explicitly simulate thermo-mechanical behavior to generate temperature-affected structural responses.

In the first category (A), several studies focus on empirically relating temperature to monitoring data, typically via regression models on long-term vibration records. A representative example is the long-term study by Liu and DeWolf on a curved post-tensioned concrete bridge, where five years of ambient vibration data are used to show that natural frequencies decrease approximately linearly with increasing in situ concrete temperature, with shifts of about 6% over a 70°F ($\approx 21^\circ\text{C}$) range; simple linear regression models are then proposed to capture this frequency-temperature dependence and to define temperature-dependent baselines for damage assessment [18]. Other works in this category can be found in [19–21].

The second category (B) comprises contributions that explicitly perform temperature compensation, i.e., they remove temperature effects from the monitoring data before damage detection task or model updating. A representative example is the temperature-based framework of Kromanis and Kripakaran, where regression models (using PCA-compressed temperature fields and support-vector regression) are trained to predict the thermal component of quasi-static response, and anomaly detection is then carried out on the residual *prediction error* signals using a signal-subtraction method and statistically derived thresholds [22]. Other works in this category fit regression models to frequency-temperature data to normalize modal frequencies to a reference temperature, or use temperature-response relations to correct identified modal properties before FE model updating and real-time damage identification, so that remaining variability is more directly attributable to structural changes rather than environmental effects [23–25].

The third category (C) groups studies that use FEMs to simulate thermo-mechanical (TM) behavior and generate temperature-affected response data. A representative example is the work of Xia et al. on the Tsing Ma Suspension Bridge, where detailed 3D thermal FE models of deck, cross frames, and tower segments are driven by measured air temperature, wind, and solar radiation to compute transient temperature fields, which are then applied to a global structural FE model to reproduce temperature-induced displacements and stresses that match GPS and strain-gauge measurements in the longitudinal and vertical directions [26]. Other works in this category use 2D or 3D thermo-mechanical FE models to reproduce realistic temperature distributions, to study temperature-dependent stresses, stiffness and boundary conditions, and to embed temperature-dependent material laws into structural simulations and damage-identification frameworks [27–34].

Despite their solid physical basis, however, these TM-based FEM approaches face practical limitations. First, they rely on accurate temperature inputs at every element, whereas field measurements typically provide only sparse thermocouple data, making full thermal-field reconstruction uncertain. Second, many TM formulations neglect thermal inertia, the lag between ambient variation and internal temperature evolution, which can strongly influence modal behavior. Third, simplified FEM representations of boundary conditions and connections cannot easily capture their true temperature-dependent stiffness. Finally, most TM relationships originate from controlled laboratory conditions and may not reflect the heterogeneous thermal environments encountered in the field. Consequently, purely TM simulations often struggle to reproduce the empirical temperature-frequency relationships observed in real bridges, motivating the need for alternative or complementary data-informed modeling strategies.

To overcome these challenges, this study introduces a data-informed temperature modeling approach that links field measurements with an updated FEM using surrogate modeling techniques. The central idea is that instead of prescribing analytical temperature laws, we let the data reveal how temperature influences the structure. Baseline measurements of the healthy structure, collected under different ambient temperatures, are used together with the FEM to learn how temperature variations affect FEM parameters such as material stiffness and boundary conditions.

Firstly, an inverse surrogate model [35] is trained to estimate the FEM parameters from the measured modal frequencies. Next, by comparing these estimated parameters with the corresponding temperature records, we build a relationship that describes how the parameters vary with temperature. This relationship automatically captures both direct temperature effects and slower variations caused by thermal inertia.

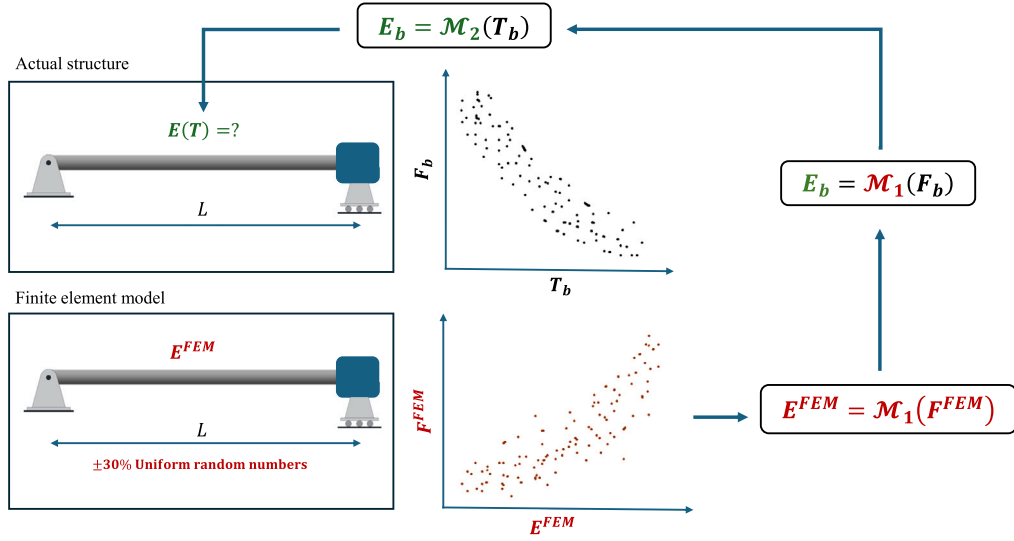


Fig. 1. The flowchart of the proposed methodology.

Once learned, the temperature-parameter relationship can be applied to the FEM to simulate damaged models under realistic temperature conditions. As a result, the synthetic modal data generated in this way reproduce the same temperature trends seen in real measurements, without needing detailed temperature fields or complex thermo-mechanical equations.

From a methodological standpoint, the contribution of this work lies in the formulation of a unified data-informed pipeline that addresses a specific open problem in vibration-based SHM: the realistic simulation of temperature effects in FEM-generated damaged data. While the individual components, namely FEM updating, inverse surrogate modeling, and neural network regression, are well established, their integration into a two-stage surrogate architecture that links field temperature measurements to effective FEM parameters through modal data has not, to the authors' knowledge, been previously explored in this form. This formulation enables the generation of synthetic modal datasets that reproduce temperature-frequency trends while preserving detectability behavior.

Building on this idea, the following sections develop, demonstrate, and validate the proposed framework. Section 2 presents the proposed methodology in detail, while Section 3 illustrates its application using a numerical example based on a 2D truss model. Section 4 applies the methodology to the publicly available experimental dataset of the KW51 bridge [36,37], combined with an updated finite element model, to evaluate its performance and accuracy on real-world data.

2. Methodology

A data-informed modeling framework is developed to capture the influence of temperature on structural dynamic properties, namely modal frequencies, using a *surrogate modeling approach*. The proposed strategy combines *baseline measurements* with a calibrated FEM of the structure to infer temperature-dependent material and boundary properties. The latter can then be used to generate reliable synthetic frequency data in simulated damage scenarios.

The overall workflow of the proposed framework is summarized in Fig. 1 and described in the following steps. Let:

$$\begin{aligned}
 \mathbf{F} &= \begin{bmatrix} f_{11} & f_{12} & \cdots & f_{1n} \\ \vdots & \vdots & \ddots & \vdots \\ f_{S1} & f_{S2} & \cdots & f_{Sn} \end{bmatrix} \\
 \mathbf{T} &= \begin{bmatrix} T_{11} & T_{12} & \cdots & T_{1m} \\ \vdots & \vdots & \ddots & \vdots \\ T_{S1} & T_{S2} & \cdots & T_{Sm} \end{bmatrix} \\
 \mathbf{E} &= \begin{bmatrix} E_{11} & E_{12} & \cdots & E_{1k} \\ \vdots & \vdots & \ddots & \vdots \\ E_{S1} & E_{S2} & \cdots & E_{Sk} \end{bmatrix}
 \end{aligned} \tag{1}$$

where, for each sample $s = 1, \dots, S$, $\mathbf{F} \in \mathbb{R}^{S \times n}$ contains the first n modal frequencies f_{si} , $\mathbf{T} \in \mathbb{R}^{S \times m}$ holds the temperature readings T_{sj} from m thermocouples, and $\mathbf{E} \in \mathbb{R}^{S \times k}$ collects the temperature-sensitive model parameters $E_{s\ell}$ for k selected quantities, such as Young's moduli, joint stiffness or boundary conditions, that vary with temperature and influence the structural dynamic response.

Step 1: Baseline data collection. The process begins with the collection of the baseline frequency and temperature data, assuming the structure in a healthy condition. The baseline denoted as $\{\mathbf{T}_b, \mathbf{F}_b\}$ characterizes the empirical relationship between ambient temperature and the modal frequencies of the structure. This dataset forms the foundation for both FEM calibration and surrogate model training.

Step 2: Finite element model updating. An initial FEM of the structure is calibrated using the baseline modal data \mathbf{F}_b to minimize the error between measured and simulated frequencies. The updated model defines the functional dependency between the model parameters and modal frequencies:

$$\mathbf{F} = \text{FEM}(\mathbf{E}) \quad (2)$$

This calibrated model serves as the numerical backbone of the proposed approach and provides the basis for generating synthetic datasets for surrogate model development.

Step 3: Inverse surrogate modeling. To estimate temperature-dependent parameters directly from modal data, an *inverse surrogate model* [35] is constructed. A large ensemble of simulations is generated by randomly varying selected temperature-sensitive parameters within realistic bounds. Specifically, for each set of parameters \mathbf{E} the modal frequencies \mathbf{F} are computed using the calibrated FEM (solving the eigenvalue problem). These bounds should be chosen wide enough to cover both modeling uncertainty and the expected temperature-induced variation of the selected parameters, but not so wide that the surrogate is trained on many practically irrelevant combinations that may reduce its accuracy in the physically meaningful range.

A regression model \mathcal{M}_1 is then trained to approximate the *inverse mapping* from modal frequencies to model parameters:

$$\mathbf{E} \approx \mathcal{M}_1(\mathbf{F}) \quad (3)$$

In essence, \mathcal{M}_1 serves as a fast, data-driven approximation of the inverse FEM operator:

$$\mathcal{M}_1 \approx \text{FEM}^{-1} \quad (4)$$

This inverse surrogate enables the efficient estimation of equivalent model properties directly from measured vibration data. It should be remarked that the number of modal frequencies at the input and the number of target model parameters should remain comparable in order to obtain a reasonably well-posed surrogate model [35].

Notably, the parameters estimated by the inverse surrogate model are best interpreted as effective temperature-sensitive quantities rather than physical properties that are uniquely identifiable in a strict inverse-problem sense. Since modal frequencies are global features, different parameter combinations may in principle produce similar modal responses, and mathematical uniqueness of the solution is not guaranteed. This is mitigated in practice by keeping the number of target parameters comparable to the number of input frequencies and by retaining only those parameters that exhibit high sensitivity to the monitored modes. Nevertheless, the objective of the framework is not the unique recovery of material properties, but the identification of an equivalent parameterization that allows the FEM to reproduce the measured temperature-dependent modal behavior. As long as the resulting synthetic data yield anomaly detection outcomes consistent with the reference or experimental data, the framework serves its intended purpose.

Step 4: Mapping temperature to material parameters. The next step aims at mapping the baseline temperature with the estimated model parameters. In particular, first the baseline frequencies \mathbf{F}_b are used in input to the inverse surrogate \mathcal{M}_1 model to estimate the corresponding parameter vectors as:

$$\mathbf{E}_b = \mathcal{M}_1(\mathbf{F}_b) \quad (5)$$

Next, these parameters are used to train a second regression model, \mathcal{M}_2 , that directly relates the baseline temperatures to these temperature-sensitive properties:

$$\mathbf{E}_b \approx \mathcal{M}_2(\mathbf{T}_b) \quad (6)$$

Model \mathcal{M}_2 thus captures a *data-driven relationship between temperature and structural properties*, combining empirical baseline data and FEM-informed synthetic information.

Step 5: Synthetic data generation and damage simulation. Once the \mathcal{M}_2 mapping is established, it can be applied to simulate healthy or damaged frequencies including temperature effects. Specifically, for a given sample of temperatures $\mathbf{T} \in \mathbb{R}^{1 \times m}$ the steps are:

1. predict the temperature-dependent material parameters as:

$$\mathbf{E} = \mathcal{M}_2(\mathbf{T}) \quad (7)$$

2. assign these parameters to the FEM;
3. introduce structural damage, e.g., localized stiffness reductions or connection weakening, to obtain the damaged FEM_d;
4. compute the modal frequencies of the damaged structure as:

$$\hat{\mathbf{F}}_d = \text{FEM}_d(\mathbf{E}) \quad (8)$$

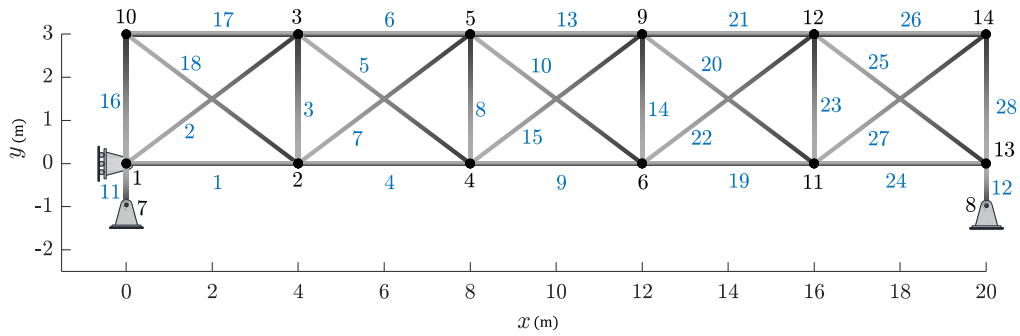


Fig. 2. The steel truss geometry, layout, and support conditions.

This process allows the generation of synthetic frequencies reflecting both mechanical damage and realistic thermal data. Such data can be used to train, validate, and benchmark SHM algorithms under conditions similar to those observed in the field.

Notably, in this study, only modal frequencies are used as inputs to the inverse surrogate. Although mode shapes could provide additional spatial information, modal frequencies were preferred because they are generally more robust and easier to identify consistently from long-term operational data, whereas reliable mode shape estimation is more sensitive to sensor density, noise, and excitation conditions.

It is worth comparing the proposed framework relative to the three categories of existing approaches reviewed in the Introduction. Empirical regression models (Category A) can capture temperature-frequency trends from monitoring data, but they are not linked to a structural model and therefore cannot generate synthetic data for unseen damage scenarios. Temperature compensation methods (Category B) remove or normalize thermal effects prior to damage detection, but they do not produce temperature-aware damaged data that could be used for threshold calibration or POD estimation. Thermo-mechanical FEM approaches (Category C) simulate thermal fields explicitly, but they require dense temperature measurements, accurate constitutive laws, and detailed boundary condition models that are rarely available in practice.

The proposed framework combines the data-driven flexibility of empirical approaches with the physical basis of FEM simulation, while avoiding the need for explicit thermal field modeling. This allows it to generate realistic temperature-dependent synthetic data for both healthy and damaged states using only sparse temperature measurements and a calibrated FEM.

3. Numerical example: planar truss

3.1. Numerical model description

We first evaluate the proposed framework on a numerical study using a planar steel truss with 28 bar elements. All elements are assumed to be made of steel with initial properties:

$$E_0 = 210 \text{ GPa}, \quad \rho_0 = 7850 \text{ kg/m}^3, \quad A_0 = 0.01 \text{ m}^2 \quad (9)$$

where E_0 is the Young's modulus, ρ_0 is the mass density, and A_0 is the cross-sectional area of each truss member in the healthy (reference) state. A schematic of the truss, including its nodal layout and support conditions, is provided in Fig. 2.

To introduce spatially varying thermal effects in a controlled way, the truss members are divided into three groups according to their position in the structure (see the color coding in Fig. 3). Elements 1-9 form group \mathcal{G}_1 (red), elements 10-18 form group \mathcal{G}_2 (purple), and the remaining elements form group \mathcal{G}_3 (yellow). Each group is assumed to be influenced by a different local temperature measurement. Specifically, we assume three thermocouples, T_1 , T_2 , and T_3 , such that T_1 affects the elements in \mathcal{G}_1 , T_2 affects the elements in \mathcal{G}_2 , and T_3 affects the elements in \mathcal{G}_3 .

For each group \mathcal{G}_i ($i = 1, 2, 3$), the effective Young's modulus is assumed to depend on the corresponding local temperature T_i according to [38]:

$$E_{\mathcal{G}_i}(T_i) = E_0 \left[1 - \frac{(T_i - 20)}{200} e^{-0.01 T_i} \right], \quad i = 1, 2, 3 \quad (10)$$

where T_i is expressed in $^{\circ}\text{C}$ and $E_{\mathcal{G}_i}(T_i)$ represents the temperature-dependent Young's modulus of all elements assigned to group \mathcal{G}_i . It should be noted that the analytical temperature-modulus relation used in this numerical example is introduced only to generate the initial healthy reference and controlled damaged datasets for verification.

3.2. Steps to build the data-informed model

Step 1 – Baseline data generation

To generate baseline (healthy) data for this numerical study, we simulate one year of environmental and operational conditions. We assume $S = 365$ samples, where each sample corresponds to one day. For each day $s = 1, \dots, S$, we assign a temperature value

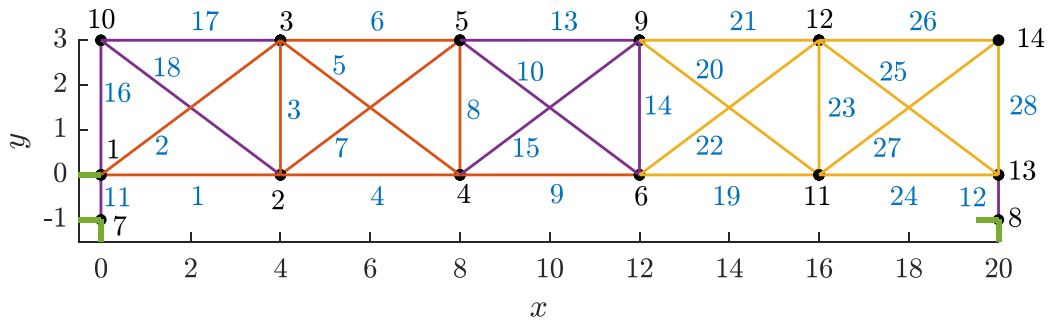


Fig. 3. The truss steel structure layout. The dimensions are in meters. The green lines represent the translational restraints.

to each thermocouple T_1 , T_2 , and T_3 . These temperatures include (i) a slow seasonal variation, (ii) a daily fluctuation, and (iii) a random component. In particular, the three temperature signals are generated as follows:

$$T_1(s) = \underbrace{15 + 15 \sin\left(\frac{2\pi s}{S}\right)}_{\text{seasonal}} + \underbrace{20 \sin\left(\frac{2\pi s}{n_d}\right)}_{\text{daily}} + \underbrace{3 \eta_1(s)}_{\text{random}} \quad (11)$$

$$T_2(s) = \underbrace{15 + 20 \sin\left(\frac{2\pi s}{S}\right)}_{\text{seasonal}} + \underbrace{16 \sin\left(\frac{2\pi s}{n_d}\right)}_{\text{daily}} + \underbrace{2 \eta_2(s)}_{\text{random}} \quad (12)$$

$$T_3(s) = \underbrace{17 + 25 \sin\left(\frac{2\pi s}{S} + \phi_Y\right)}_{\text{seasonal (phase-shifted)}} + \underbrace{20 \sin\left(\frac{2\pi s}{n_d} + \phi_D\right)}_{\text{daily (phase-shifted)}} + \underbrace{8 \eta_3(s)}_{\text{random}} \quad (13)$$

where n_d is the effective number of samples per daily cycle (e.g., $n_d = 1$ if one sample is taken per day, or $n_d = 24$ if hourly data are later used), $\eta_i(s)$ is zero-mean Gaussian noise, and ϕ_Y , ϕ_D are phase shifts added to T_3 to model spatial/thermal lag in that region of the structure. The temperature matrix is then collected as:

$$\mathbf{T}_b = \begin{bmatrix} T_1(1) & T_2(1) & T_3(1) \\ \vdots & \vdots & \vdots \\ T_1(S) & T_2(S) & T_3(S) \end{bmatrix} \in \mathbb{R}^{S \times 3} \quad (14)$$

For each sample s , the temperature-dependent Young's moduli $E_{G_1}(T_1(s))$, $E_{G_2}(T_2(s))$, and $E_{G_3}(T_3(s))$ are assigned to the corresponding element groups in the truss model via Eq. (10). The resulting truss stiffness matrix is then assembled, and an eigenvalue analysis is performed to compute the undamped natural frequencies of the structure. We retain the first 6 modal frequencies, and to include measurement uncertainty, we corrupt each simulated modal frequency with additive noise at 1% level. The resulting frequency matrix is:

$$\mathbf{F}_b = \begin{bmatrix} f_{b1}(1) & \dots & f_{b6}(1) \\ \vdots & \ddots & \vdots \\ f_{b1}(S) & \dots & f_{b6}(S) \end{bmatrix} \in \mathbb{R}^{S \times 6} \quad (15)$$

Fig. 4 illustrates the generated baseline data. Subplot (a) shows the three synthetic temperature histories T_1 , T_2 , and T_3 over the simulated year, subplot (b) shows the relationship defined in Eq. (10), i.e., the effective Young's modulus $E_{G_i}(T_i)$ for each element group G_i as a function of its assigned temperature T_i , and subplot (c) shows the first 6 natural frequencies (on a logarithmic scale) obtained from the eigenvalue analysis as temperature varies.

Step 2 – Model updating

Since this analysis is numerical and the reference parameters are known, model updating is not required. The original finite element model is therefore used as the updated model representing the healthy baseline configuration.

Notably, in practical applications (such as the next case study), possible mismatch between the FEM and the real structure is addressed through model updating. Therefore, this numerical example should be interpreted as a verification case; for a broader discussion, please refer to [15].

Step 3 – Inverse surrogate model

To construct the inverse surrogate model, we select four temperature-sensitive parameters from the updated finite element model corresponding to distinct structural groups:

$$\mathbf{E} = [E_l, E_t, E_d, E_v]$$

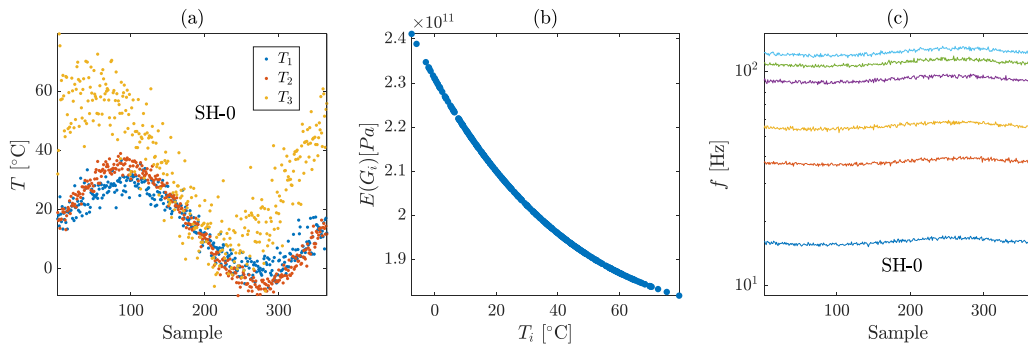


Fig. 4. Baseline simulation results for the planar truss example. (a) Synthetic temperature variations T_1 , T_2 , and T_3 over one simulated year. (b) Temperature-dependent Young's moduli $E_{G_i}(T_i)$ for the three element groups G_1 - G_3 , as defined in Eq. (10). (c) First 6 natural frequencies obtained from eigenvalue analysis under the varying temperature conditions, plotted on a logarithmic scale.

Table 1

Architecture and training configuration of the inverse surrogate DNN model.

Component	Description
Input layer	Feature input layer with dimension equal to the number of modal frequencies ($n = 6$).
Dropout layer	Dropout rate of 0.05 applied after input to improve generalization.
Hidden layers	Fully connected layers with [128, 128, 64, 64, 32, 16] neurons, each followed by ReLU activation.
Output layer	Fully connected layer with 4 neurons corresponding to E_l , E_t , E_d , and E_v .
Optimizer	Adam optimizer with learning rate 0.001 and piecewise schedule.
Loss function	Mean squared error (MSE).
Training setup	1000 epochs, GPU execution, 80/20 train-test split.

where E_l , E_t , E_d , and E_v represent the effective Young's moduli of the lower (1, 4, 9, 19, 24), top (17, 6, 13, 21, 26), diagonal (2, 18, 7, 5, 15, 10, 20, 22, 25, 27), and vertical members (16, 3, 8, 14, 23), respectively.

To generate the training data for the surrogate model, these four parameters are randomly varied within $\pm 20\%$ of their nominal values (210 GPa), producing 1000 uniformly distributed samples of \mathbf{E} . The $\pm 20\%$ bounds were selected to cover the expected temperature-induced variation while avoiding an unnecessarily large parameter space in this controlled numerical example. For each sampled set of parameters, the truss eigenvalue problem is solved to obtain the first 6 natural frequencies, $\mathbf{F} = [f_1, f_2, f_3, f_4, f_5, f_6]$. The dataset pairs $\{\mathbf{F}, \mathbf{E}\}$ are then used to train a deep neural network (DNN) acting as the inverse surrogate model $\mathbf{E} \approx \mathcal{M}_1(\mathbf{F})$, where \mathcal{M}_1 approximates the inverse FEM operator and predicts the temperature-sensitive parameters from the modal frequency vector.

The dataset is split into 80% for training and 20% for testing. The DNN is trained using the Adam optimizer [39] with a mean-squared-error (MSE) loss function and an initial learning rate of 10^{-3} for up to 1000 epochs. The network is implemented and trained on a GPU to accelerate convergence. Table 1 summarizes the adopted network configuration.

Since the input dimension is small (6 modal frequencies) and the output dimension is moderate (4 effective stiffness parameters), a fully connected network was considered sufficient to represent the nonlinear frequency-parameter relationship. The gradually decreasing hidden layer sizes [128, 128, 64, 64, 32, 16] were chosen to provide enough capacity in the first layers to capture global nonlinear interactions among modal frequencies, while progressively compressing the representation toward the lower-dimensional parameter space. ReLU activation was adopted because of its stable optimization properties and widespread use in regression problems of this type.

A small dropout rate of 0.05 was introduced only after the input layer to mildly regularize the model and reduce the risk of overfitting, while preserving the relationships embedded in the numerical dataset. The Adam optimizer with an initial learning rate of 10^{-3} was selected as a robust default choice for nonlinear regression, providing stable convergence across repeated trials.

After training, the inverse surrogate is evaluated on the 20% test dataset. Fig. 5 shows the prediction performance in terms of root-mean-square error (RMSE) for each element. Elements that contribute more significantly to the global stiffness, particularly the diagonal members, exhibit lower prediction errors (darker shades), showing that the inverse surrogate captures the dominant stiffness-frequency relationships effectively.

Step 4 – Mapping temperature to material parameters

In this step, we link temperature measurements to equivalent stiffness parameters. The first operation is to apply the inverse surrogate model \mathcal{M}_1 (trained in Step 3) to the baseline frequency data (obtained in Step 1). Specifically, the baseline samples of the first 6 modal frequencies ($\mathbf{F}_b \in \mathbb{R}^{365 \times 6}$) are passed through \mathcal{M}_1 to estimate the corresponding effective stiffness parameters:

$$\mathbf{E}_b = \mathcal{M}_1(\mathbf{F}_b), \quad \mathbf{E}_b = \begin{bmatrix} E_{bl} & E_{bt} & E_{bd} & E_{bv} \end{bmatrix} \quad (16)$$

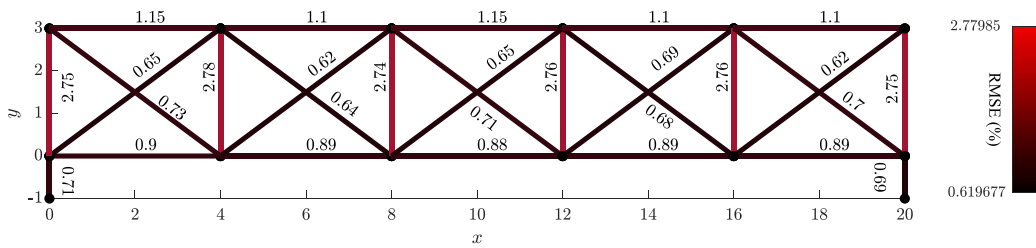


Fig. 5. Performance of the inverse surrogate model evaluated on the 20% testing dataset. The color map represents the root-mean-square error (RMSE) of the predicted elastic moduli for each truss element. Red regions indicate higher prediction errors, while darker tones correspond to lower errors.

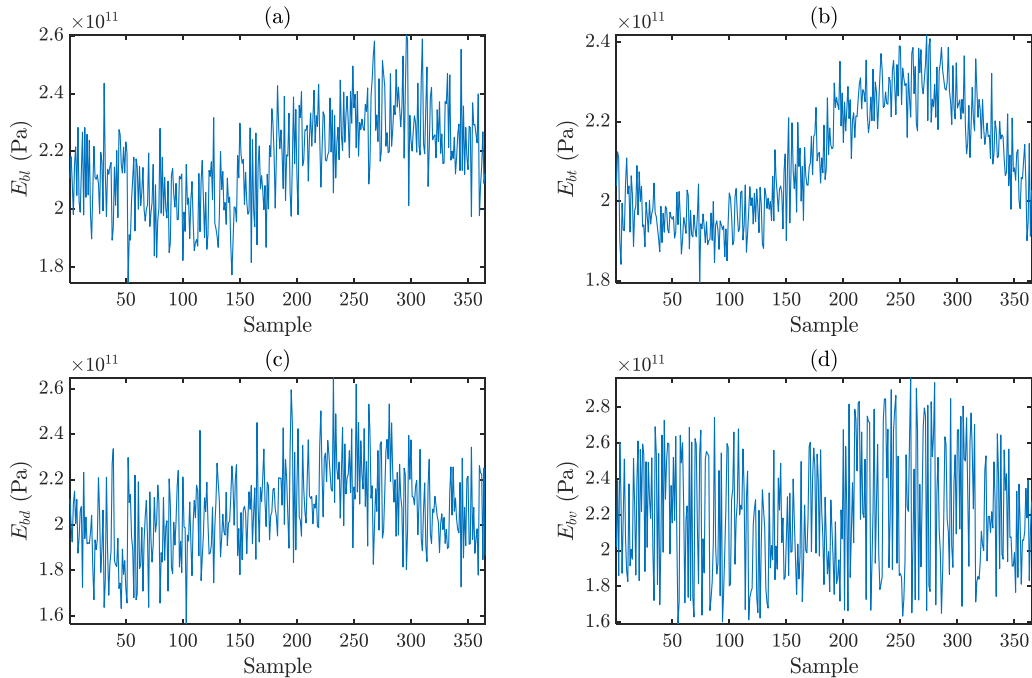


Fig. 6. Estimated baseline variations of equivalent Young's moduli obtained using the inverse surrogate model \mathcal{M}_1 . Each subplot corresponds to one of the four structural groups: (a) lower elements (E_{bl}), (b) top elements (E_{bt}), (c) diagonal elements (E_{bd}), and (d) vertical elements (E_{bv}).

where E_{bl} , E_{bt} , E_{bd} , and E_{bv} denote the predicted Young's moduli associated with the lower, top, diagonal, and vertical groups of elements, respectively, related to the baseline dataset. These four trajectories are shown in Fig. 6, subplots (a)–(d).

Next, using the baseline temperature variations \mathbf{T}_b , the second DNN regression model \mathcal{M}_2 (Eq. (6)) is constructed to capture the relationship between temperature and the estimated moduli of elasticity \mathbf{E}_b . This model has the same architecture and training settings as \mathcal{M}_1 (see Table 1), except that the input layer has three neurons corresponding to the three temperature sensors.

Step 5 – Verification using healthy and damaged data

To verify the proposed framework, both healthy and damaged structural states are simulated using the planar truss model. The baseline (healthy) configuration is denoted as SH-0, and three damage scenarios are introduced by reducing the cross-sectional areas of specific element groups by 50%. The damage cases are defined as follows:

- SB-50: bottom elements (1, 4, 9, 19, 24) reduced by 50% in cross-sectional area;
- ST-50: top elements (17, 6, 13, 21, 26) reduced by 50%;
- SD-50: diagonal elements (2, 5, 7, 10, 15, 18, 20, 22, 25, 27) reduced by 50%.

Together with the healthy case, these configurations yield a total of four structural states (SH-0, SB-50, ST-50, and SD-50).

A synthetic temperature record with daily variation is generated for the three thermocouples T_1 , T_2 , and T_3 , using the same formulation described previously (Eqs. (11), (12), and (13)), for a total duration of 4 years, with each year corresponding to one structural condition: the first 365 samples represent SH-0, the next 365 for SB-50, followed by ST-50, and finally SD-50. The

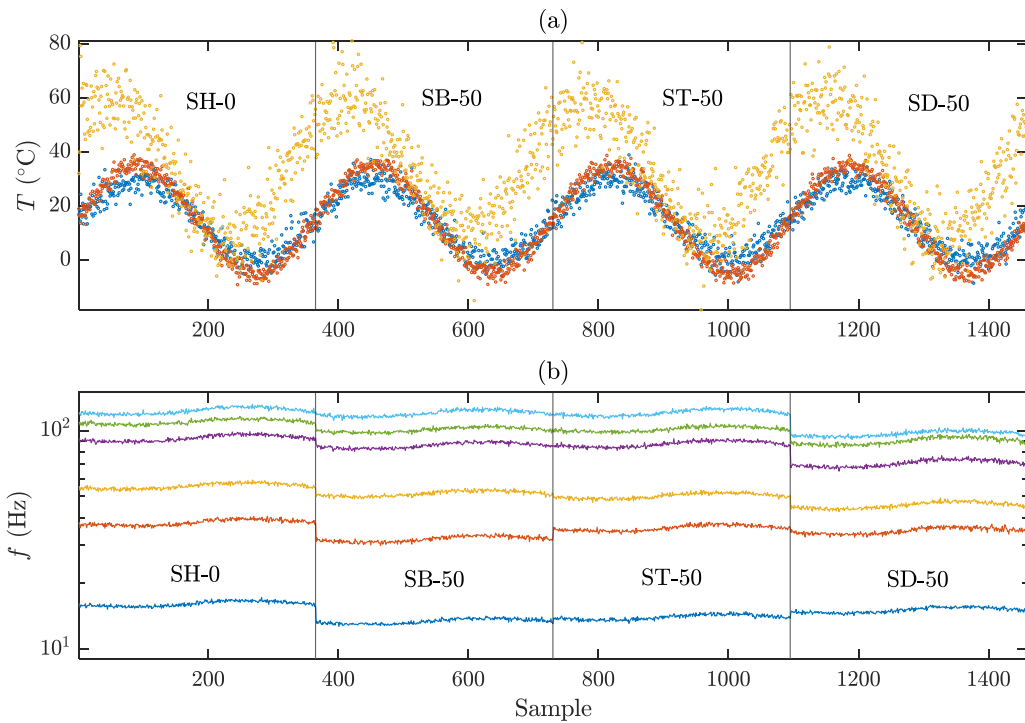


Fig. 7. Dataset generated for healthy and damaged truss. (a) Simulated temperature histories of the three thermocouples T_1 , T_2 , and T_3 over a four-year period, where each year corresponds to one structural state. (b) Corresponding first 6 natural frequencies obtained from eigenvalue analyses of the temperature-dependent FEM for all four scenarios, shown on a logarithmic scale.

temperature matrix therefore contains $n_t = 4 \times 365 = 1460$ samples. Notably, since the temperature histories in Eqs. (11)–(13) include a random component, the four yearly cycles are not identical.

For each temperature instance $s = 1, 2, \dots, 1460$, the Young's modulus of every element is adjusted according to the temperature-stiffness relationship of Eq. (10), the global stiffness and mass matrices are assembled, and the eigenvalue problem is solved to extract the first 6 natural frequencies. To apply measurement noise, 1% Gaussian perturbations are added to each simulated frequency.

The resulting dataset thus contains temperature and modal information for all four structural states under realistic thermal variation. Fig. 7 illustrates the generated data: subplot (a) shows the temperature histories of the three thermocouples over the four-year simulation, while subplot (b) presents the corresponding first 6 natural frequencies on a logarithmic scale. These datasets serve as the ground truth to evaluate the performance of model \mathcal{M}_2 .

For this evaluation, the four-year temperature variations $\mathbf{T}_t \in \mathbb{R}^{1460 \times 3}$ are provided as input to \mathcal{M}_2 . For each temperature sample, the model predicts the corresponding effective Young's moduli:

$$\mathbf{E}_t = \mathcal{M}_2(\mathbf{T}_t) \quad (17)$$

where $\mathbf{E}_t = [E_{tl}, E_{tt}, E_{td}, E_{tw}]$ represents the estimated Young's moduli for the lower, top, diagonal, and vertical element groups, respectively. These temperature-dependent properties are then applied to the updated FEM to reconstruct the structural response. For each sample, the corresponding modal frequencies are computed as:

$$\hat{\mathbf{F}}_t = \text{FEM}(\mathbf{E}_t, \text{damage}) \quad (18)$$

The eigenvalue problem is solved for each sample to extract the first 6 natural frequencies, and 1% Gaussian noise is added to emulate measurement uncertainty.

The predicted modal frequencies $\hat{\mathbf{F}}_t$ are then compared with the ground truth modal data \mathbf{F}_t to evaluate the predictive accuracy of the proposed framework. Fig. 8(a)–(f) illustrates this comparison for the first 6 natural frequencies, f_1 to f_6 , respectively, where the blue curves represent the actual (ground truth) modal frequencies and the red curves correspond to the predictions obtained from the surrogate model \mathcal{M}_2 .

The predictive accuracy is quantitatively assessed using the Mean Absolute Percentage Error (MAPE) for each scenario and mode, defined as:

$$\text{MAPE} = \frac{100}{S} \sum_{s=1}^S \left| \frac{f_i(s) - \hat{f}_i(s)}{f_i(s)} \right| \quad (19)$$

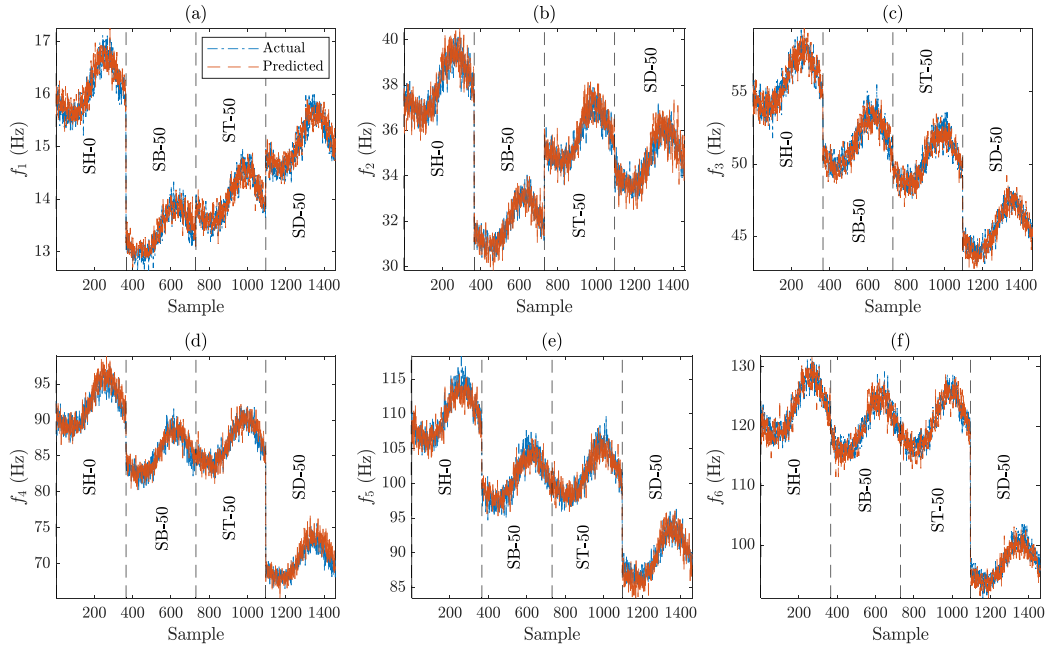


Fig. 8. Comparison between ground truth and predicted modal frequencies for the verification dataset. Subplots (a)–(f) correspond to the first 6 natural frequencies (f_1 – f_6), respectively. Blue curves represent the ground truth frequencies F_i , while red curves indicate the predictions \hat{F}_i , obtained from \mathcal{M}_2 .

Table 2

MAPE [%] of predicted modal frequencies compared with the ground truth for each structural scenario, together with the average values over all scenarios.

Scenario	MAPE [%]					
	f_1	f_2	f_3	f_4	f_5	f_6
SH-0	1.17	1.21	1.13	1.25	1.20	1.19
SB-50	1.30	1.29	1.36	1.28	1.41	1.34
ST-50	1.32	1.39	1.34	1.25	1.35	1.24
SD-50	1.41	1.50	1.29	1.64	1.57	1.37
Average	1.30	1.35	1.28	1.35	1.38	1.28

where $f_i(s)$ and $\hat{f}_i(s)$ denote the actual and predicted modal frequencies, and $S = 365$ is the total number of samples in each scenario. Table 2 summarizes the obtained MAPE values for the first 6 natural frequencies.

Across all modes, a close agreement is observed between the two sets of curves as the average error values remain below 1.39%, confirming that the proposed method and model \mathcal{M}_2 accurately captured the temperature-frequency relationship under both healthy and damaged conditions.

3.3. Verification by damage detection

Beyond reproducing modal frequency trends, a central objective of the proposed framework is the generation of synthetic data that preserve the detectability needed for threshold calibration, PFA and POD estimation, and MDD assessment under realistic temperature variability. The following analysis evaluates whether this objective is met by comparing the anomaly detection outcomes obtained from the data-informed datasets with those from the reference thermo-mechanical model.

To this end, a Mahalanobis distance-based damage index (DI) is built to evaluate whether the proposed data-informed framework yields, under varying temperature conditions, the same *false-alarm* and *damage-detection* behavior as those obtained using the reference thermo-mechanical model in the simulations of modal data. In particular, the frequencies of the healthy dataset SH-0, generated using the thermo-mechanical relationship described in Step 1, are taken as baseline and their mean vector $\mu_b \in \mathbb{R}^{1 \times 6}$ and covariance matrix $\Sigma_b \in \mathbb{R}^{6 \times 6}$ are used to build the Mahalanobis-based damage index (DI) as:

$$DI(s) = \sqrt{(\mathbf{f}(s) - \mu_b) \Sigma_b^{-1} (\mathbf{f}(s) - \mu_b)^T} \quad (20)$$

for any sample of modal frequencies $\mathbf{f}(s) \in \mathbb{R}^{1 \times 6}$.

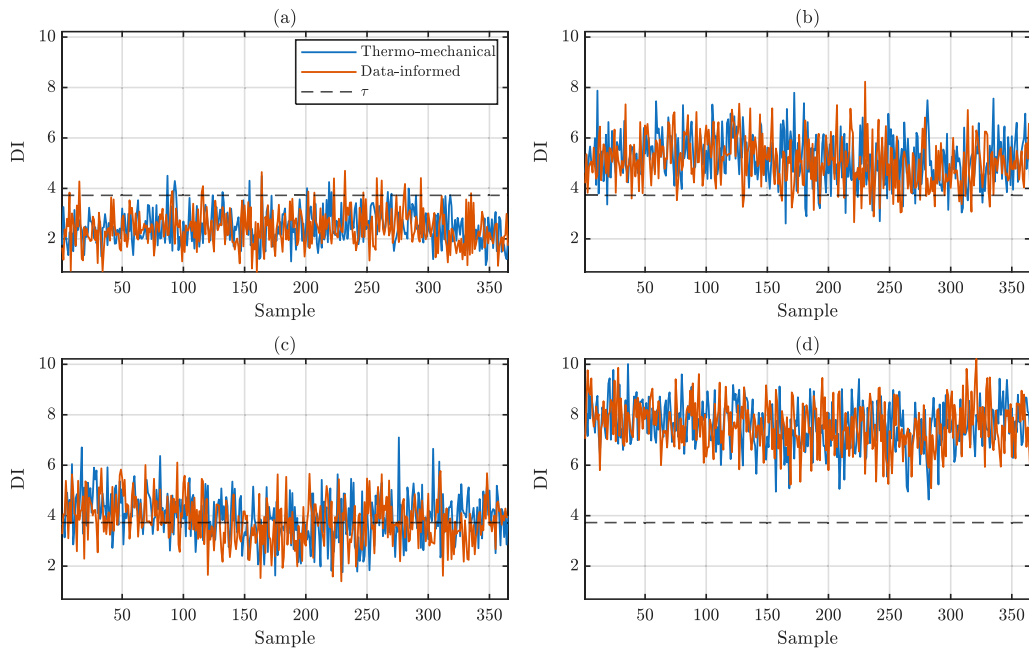


Fig. 9. Comparison of damage index responses computed with respect to the healthy baseline for unseen test datasets. Subplots correspond to: (a) SH-0, (b) SB-20, (c) ST-20, and (d) SD-20. Blue and red lines correspond to thermo-mechanical and data-informed DIs, respectively, and the black dashed line represents τ .

Next, to avoid data leakage, the datasets used for evaluation are fully separated from the healthy dataset SH-0 employed to train the proposed data-informed model \mathcal{M}_2 . Specifically, an additional unseen temperature history is generated using the same definitions of Eqs. (11)–(13), but with a different realization of the random component, leading to values different from that used in Step 1. This temperature history is used to produce (i) two healthy test datasets, one generated using the reference thermo-mechanical relationship and one generated using the proposed data-informed framework; (ii) thirty damaged test datasets, 15 of them generated using the reference thermo-mechanical relationship and 15 generated using the proposed data-informed framework. In particular, five damage severity levels for each damage scenarios {SB-10, SB-20, SB-30, SB-40, SB-50, ST-10, ST-20, ST-30, ST-40, ST-50, SD-10, SD-20, SD-30, SD-40, SD-50} were considered to assess the damage detection sensitivity using the proposed approach.

Fig. 9 compares the DI responses obtained using the frequency datasets built on the thermo-mechanical relation (blue) and on the data-informed model (red) for the healthy condition (subplot a), and for three representative moderate damage scenarios, namely SB-20, ST-20, SD-20 (subplots b, c, and d). In each subplot, the horizontal black dashed line indicates the threshold τ obtained as the 98th percentile of the baseline DI values.

The close agreement between the ground truth and data-informed DIs shows that the proposed framework preserves the detection behavior associated with the thermo-mechanical model, not only in the undamaged state but also for representative damage cases from all three structural families.

To further examine sensitivity to damage severity, Fig. 10 presents the DI results for one representative damage family, namely the bottom-chord cases {SH-0, SB-10, SB-20, SB-30, SB-40, SB-50}.

As expected, detectability increases with increasing damage severity. Importantly, the same trend is reproduced by the data-informed model, indicating that it captures not only severe damage-induced deviations but also the transition from weakly detectable to clearly detectable damage under temperature-varying conditions.

Results for all considered cases are summarized in Table 3 in terms of PFA and POD [10]. For the healthy case, the PFA obtained with the data-informed model is 4.38%, compared with 4.11% for the thermo-mechanical reference, resulting in a very small absolute difference of 0.27 percentage points. This indicates that the proposed method did not introduce excessive false positives relative to the baseline statistics.

For the damaged cases, the POD values obtained from the data-informed synthetic data closely follow those of the thermo-mechanical datasets over a broad range of damage severities. For bottom-chord damage, the POD rises from 26.03% at SB-10 to 92.33% at SB-20 and reaches 100% from SB-30 onward in the data-informed case, closely matching the thermo-mechanical reference. For top-chord damage, the corresponding increase is more gradual, from 7.40% at ST-10 to 53.97% at ST-20 and 97.26% at ST-30, before reaching 100% at ST-40 and ST-50. For diagonal-member damage, even the smallest considered case SD-10 already achieves a POD of 66.30% in both models, and full detection is reached from SD-20 onward.

The results show that the proposed data-informed framework preserves damage information while adding thermal effects, rather than merely matching average modal trends.

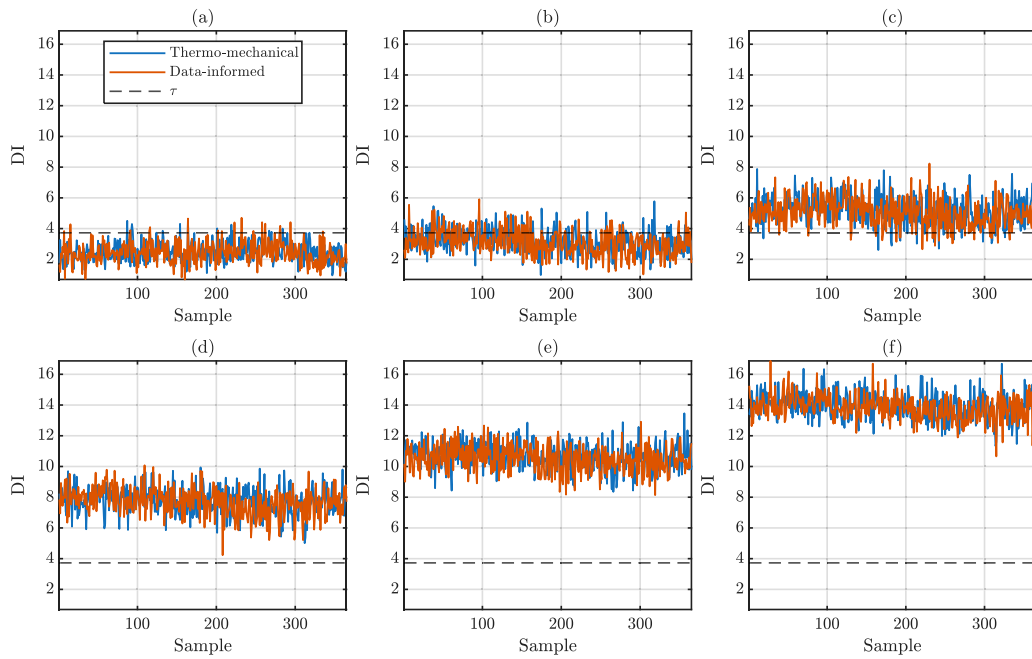


Fig. 10. Damage index sensitivity analysis for the bottom-chord damage family. Subplots correspond to: (a) SH-0, (b) SB-10, (c) SB-20, (d) SB-30, (e) SB-40, and (f) SB-50. Blue and red lines correspond to thermo-mechanical and data-informed DIs, respectively, and the black dashed line represents τ .

Table 3

Comparison of PFA and POD obtained from the thermo-mechanical ground truth datasets and the data-informed synthetic datasets using a common τ .

Scenario	Metric	Thermo-mechanical [%]	Data-informed [%]	Abs. diff. [%]
SH-0	PFA	4.11	4.38	0.27
SB-10	POD	26.03	21.64	4.38
SB-20	POD	94.79	92.33	2.47
SB-30	POD	100.00	100.00	0.00
SB-40	POD	100.00	100.00	0.00
SB-50	POD	100.00	100.00	0.00
ST-10	POD	12.60	7.40	5.21
ST-20	POD	59.73	53.97	5.75
ST-30	POD	98.08	97.26	0.82
ST-40	POD	100.00	100.00	0.00
ST-50	POD	100.00	100.00	0.00
SD-10	POD	66.30	66.30	0.00
SD-20	POD	100.00	100.00	0.00
SD-30	POD	100.00	100.00	0.00
SD-40	POD	100.00	100.00	0.00
SD-50	POD	100.00	100.00	0.00

The results also provide insight into the relative detectability of different damage locations. Bottom-chord and diagonal-member damages are more detectable at low severities than top-chord damage, indicating that these element groups have a stronger influence on the first six modal frequencies under the adopted structural configuration. In particular, the diagonal damage family shows the highest sensitivity, with SD-10 already producing a POD above 66%, whereas top damage remains more difficult to detect at the same severity. This suggests that, for this truss, diagonal and bottom members contribute more strongly to the global stiffness patterns captured by the monitored modes, while top-member damage may induce modal changes that are partially masked by temperature-induced variability at low damage levels.

The results also highlight an expected limitation. For the smaller damage levels, especially SB-10 and ST-10, the separation between healthy and damaged distributions is weaker because the damage-induced changes approach the magnitude of temperature-induced variability. This motivates the definition of minimum detectable damage (MDD) [40], as the smallest damage level leading to a favorable POD under realistic temperature variability. Adopting a POD of 90% as a reliable detectability level, the results indicate that the MDD is about 30% for SB and ST scenarios, and about 20% for the SD scenario.

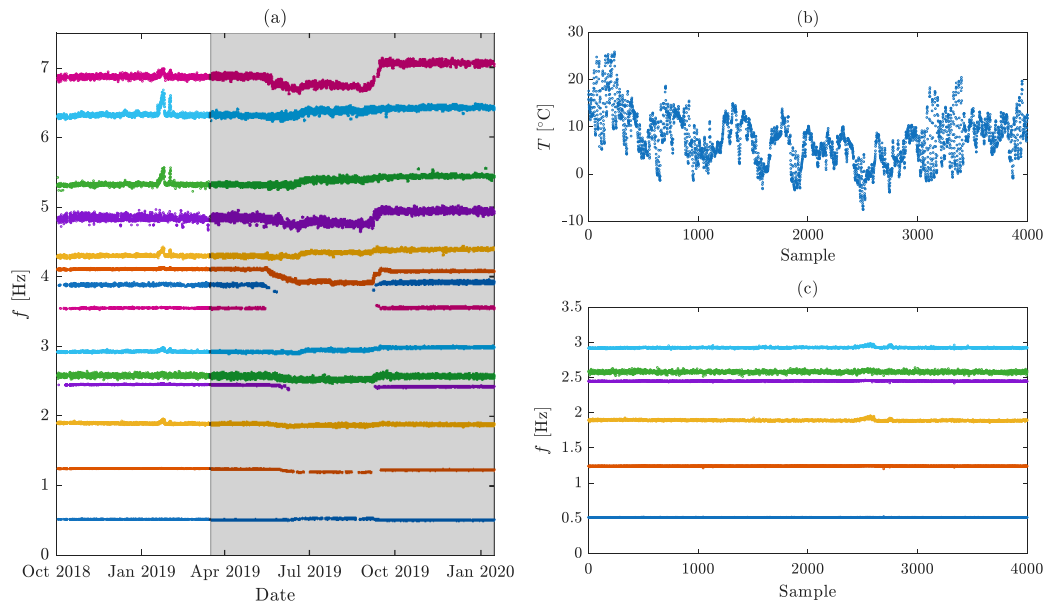


Fig. 11. (a) Time histories of the 14 identified modal frequencies of the KW51 bridge [41]. (b) Processed temperature measurements from the single sensor installed before retrofit. (c) Processed time histories of the first 6 modal frequencies. Missing data in panels (b) and (c) were filled using the k -NN imputation method ($k = 10$).

Therefore, the present analysis should not be interpreted as evidence of universal separability between temperature and damage. Rather, it demonstrates that the proposed framework can reproduce the same *detectability regime* as the reference model, including the reduced detectability of milder damage under realistic thermal fluctuations.

It should be noted that the MDD values reported above are specific to the truss configuration considered, the set of monitored modes, and the adopted detection threshold. In general, the MDD is expected to vary across structures, sensor configurations, and damage locations, and should therefore be interpreted as a case-specific metric rather than a universal quantity.

4. Experimental study: KW51 railway bridge

4.1. Bridge description and monitoring data

The KW51 bridge is a steel single-span tied-arch railway bridge with a two-track deck, measuring 115 m in length and 12.4 m in width. The deck is suspended from the main arch by a series of diagonal elements. Between May 15 and September 27, 2019, the bridge underwent a retrofitting operation to correct a detected construction error [36,37].

The available monitoring dataset covers three distinct periods:

- 7.5 months before the retrofit (October 2, 2018–May 15, 2019);
- 4.4 months for the entire retrofit period (May 15–September 27, 2019);
- 3.5 months after the retrofit (September 27, 2019–January 15, 2020).

Ambient vibration data were continuously collected at an hourly rate. Modal identification was performed using the covariance-driven stochastic subspace identification (SSI-COV/REF) method [41]. As shown in Fig. 11(a), 14 modal frequencies were extracted from 5-min ambient vibration recordings, measured by 12 uniaxial accelerometers installed on both the deck and arch of the bridge, with vertical and transverse orientations.

4.2. Steps to construct the data-informed model

Step 1 – Baseline dataset

To build the baseline, only the data acquired *before the retrofit* are used. The first 6 modal frequencies are selected as the target variables for the temperature-frequency modeling, denoted as:

$$\mathbf{F}_{\text{Exp}} = [f_{b1}, f_{b2}, f_{b3}, f_{b4}, f_{b5}, f_{b6}]$$

A single thermocouple, labeled *tBD31A* [36], was installed beneath the bridge deck to measure the steel temperature. The temperature input is therefore a *structural* temperature measurement, not ambient air temperature. Temperature measurements

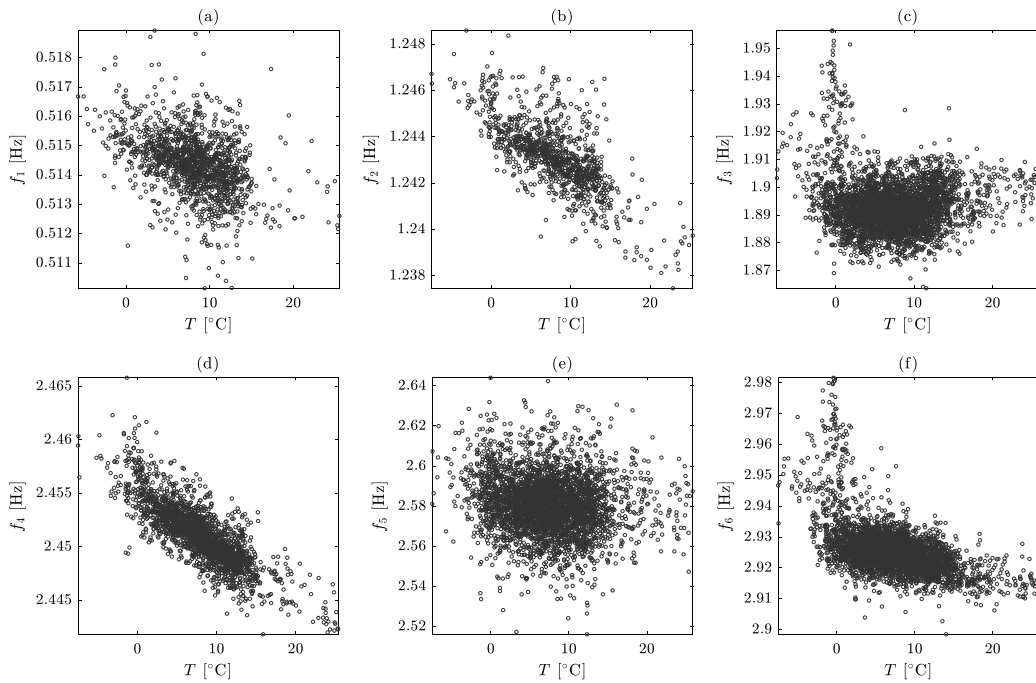


Fig. 12. Identified natural frequencies of the KW51 railway bridge vs. ambient temperature for the first 6 modes.

were recorded at the same sampling rate as the modal frequencies, ensuring correspondence between thermal and modal data. To account for thermal inertia effects, a *lagged temperature dataset* was generated by introducing 23 lagged values in addition to the current measurement, forming a 24-dimensional temperature feature vector:

$$\mathbf{T}_b = [T_b(t), T_b(t-1), \dots, T_b(t-23)]$$

The lag length of 24 h was selected to cover one full daily temperature cycle and thereby capture short-term thermal inertia effects in the structure. This choice is also consistent with [42], where the influence of lag length on temperature-frequency regression was investigated for the KW51 bridge, and 24 lagged values were found to provide satisfactory predictive performance.

Both the temperature and modal frequency records contain missing entries and to handle these gaps, the k-Nearest Neighbors (*k*-NN) [43] imputation method was applied with $k = 10$ to reconstruct the missing data points. After preprocessing, the first 4000 samples were retained for analysis. Fig. 11(b) shows the temperature time series, and Fig. 11(c) displays the 6 modal frequencies. These serve as the experimental baseline data for training and validating the proposed framework.

Notably, Figs. 12(a)–(f) illustrate the relationship between the first 6 identified modal frequencies (non-imputed) of the KW51 bridge and the measured structural temperature during the pre-retrofitting monitoring period (first 4000 samples). A linear temperature-frequency dependence can be observed for most modes. However, pronounced peaks appear in modes 3 and 6 during January 2019, when temperatures dropped below 0 °C, leading to a sudden increase in corresponding modal frequencies. This behavior, as reported in [44], shows a bilinear frequency-temperature relationship with a distinct knee point around 0 °C, attributed to frost-induced stiffening of the porphyry ballast layer supporting the tracks.

The existence of these below-zero frequency peaks is therefore critical from an SHM point of view, as they can easily be misinterpreted as damage-induced stiffness changes if temperature effects are not properly accounted for, leading to an increased probability of false alarms.

Step 2 – FEM development and updating

A detailed discussion on the finite element model development and updating of the KW51 bridge is presented in Appendix A.

Step 3 – Surrogate modeling

Parameters and sampling. The updated finite element model obtained in Step 2 serves as the reference numerical model for surrogate data generation. Among all calibrated parameters in Step 2 (see Table A.4), only those expected to vary with temperature are retained as follows:

$$\mathbf{E} = [E_{\text{bot}}, E_{\text{arc}}, E_{\text{br}}, E_{\text{con}}, E_{\text{pip}}] \quad (21)$$

Table 4
Architecture and training settings of the inverse surrogate model \mathcal{M}_1 .

Component	Details
Training/Test split	80%/20%
Input layer	6 neurons (modal frequencies)
Hidden layer 1	256 units, activation: ReLU
Hidden layer 2	128 units, activation: ReLU
Hidden layer 3	64 units, activation: ReLU
Hidden layer 4	32 units, activation: ReLU
Hidden layer 5	16 units, activation: ReLU
Output layer	5 neurons (elastic moduli)
Loss function	Mean Squared Error (MSE)
Optimizer	Adam (LR = 0.001)
Epochs/Batch size	1000/128
Standardization	Applied to both inputs and outputs

Table 5
Mean Absolute Percentage Error (MAPE) of the inverse surrogate model \mathcal{M}_1 evaluated on the 20% testing dataset.

Parameter	E_{bot}	E_{arc}	E_{br}	E_{con}	E_{pip}
MAPE [%]	0.0275	0.0264	0.0176	0.0261	0.0201

where E_{bot} , E_{arc} , E_{br} , E_{con} , and E_{pip} represent the effective elastic moduli of the bottom, arch, brace, connection, and transverse pipe elements, respectively. Geometric and mass-related parameters are excluded, as they remain constant under normal seasonal temperature variations.

To construct a representative dataset, 1000 uniformly distributed samples are generated for each of the five parameters using $\pm 30\%$ bounds around their updated mean values. The $\pm 30\%$ bounds were adopted to account for the uncertainty observed between the numerical model and the actual structure, while still keeping the sampling domain within a practically meaningful range [45]. A PYTHON script was developed to perform this sampling using the SAP2000 Open Application Programming Interface (OAPI), which enables bidirectional communication with the SAP2000 model.

Each sampled parameter set is applied to the FEM via the OAPI interface, the eigenvalue problem is solved, and the first 6 modal frequencies are extracted. Repeating this procedure 1000 times yields the dataset $\{\mathbf{E}, \mathbf{F}\}$, with:

$$\mathbf{F} \in \mathbb{R}^{1000 \times 6}, \quad \mathbf{E} \in \mathbb{R}^{1000 \times 5}$$

Building the inverse surrogate model. The generated dataset is used to train the neural network surrogate model \mathcal{M}_1 that maps the modal frequencies to their corresponding stiffness parameters ($\mathbf{E} \approx \mathcal{M}_1(\mathbf{F})$). The network is implemented in PYTHON using the TensorFlow library, and trained with 80% of the data for training and 20% for testing. The model architecture and training configuration are summarized in Table 4.

The architecture of \mathcal{M}_1 was selected according to the dimensionality of the data. The input vector contains only 6 modal frequencies, whereas the output consists of 5 effective stiffness parameters. A fully connected network was therefore adopted as a suitable structure for this low-dimensional nonlinear task. Compared with the numerical truss example, a slightly wider first hidden layer was used in order to capture the more complex parameter interactions associated with the bridge FEM and the larger variability of the sampled parameter space. The progressive reduction of layer widths from 256 to 16 neurons acts as a nonlinear compression from modal space to parameter space and was found to provide stable training and accurate prediction.

ReLU activation was used in all hidden layers because of its favorable optimization behavior in deep regression networks. The Adam optimizer and MSE loss were selected as a robust combination for continuous-output regression.

After training, \mathcal{M}_1 is evaluated using the 20% test dataset. The prediction accuracy is quantified through MAPE between the predicted and true parameter values, with results summarized in Table 5 and shown in Fig. 13. These results confirm that the model achieves excellent predictive performance, with MAPE values below 0.03% for all parameters, demonstrating that the surrogate captures the nonlinear relationship between modal frequencies and stiffness parameters with high fidelity.

Step 4 – Predicting experimental observations

The trained inverse surrogate model \mathcal{M}_1 is next applied to the 4000 experimental modal frequency samples obtained from continuous monitoring of the KW51 bridge. Before prediction, a bias alignment is applied to ensure that the mean experimental modal frequencies match those of the updated FEM. This step is necessary because even after model updating, small systematic differences remain between the numerical and experimental mean frequencies [15]. The aligned experimental modal frequencies are therefore computed as:

$$\mathbf{F}_b = \mathbf{F}_{\text{Exp}} - \mu[\mathbf{F}_{\text{Exp}}] + \mu[\mathbf{f}_{\text{Num}}] \quad (22)$$

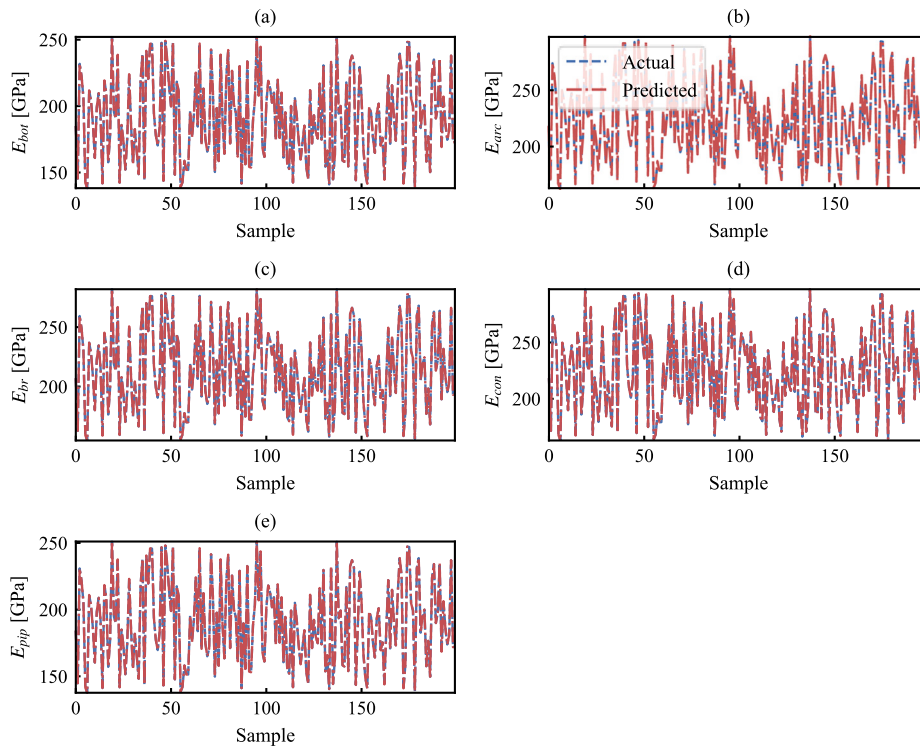


Fig. 13. Performance of the trained inverse surrogate model \mathcal{M}_1 evaluated on the testing dataset. The predicted versus true elastic modulus values are shown for (a) E_{bot} , (b) E_{arc} , (c) E_{br} , (d) E_{con} , and (e) E_{pip} .

where $\mu[\cdot]$ denotes the mean operator, and \mathbf{F}_{Exp} is the experimental modal frequency matrix, and \mathbf{f}_{Num} is the numerical modal frequency vector, respectively.

This bias alignment step is introduced to remove the residual mean offset between the updated FEM and the experimental baseline data before applying the inverse surrogate model. Its purpose is only to make the numerical and experimental modal frequency domains comparable, and assumes that the remaining discrepancy between the model and the real structure can be approximated mainly as a mean frequency offset.

Next, the aligned frequencies \mathbf{F}_b are provided as input to the inverse surrogate model \mathcal{M}_1 to estimate the effective elastic moduli:

$$\mathbf{E}_b = \mathcal{M}_1(\mathbf{F}_b) \quad (23)$$

resulting in 4000 samples of temperature-dependent equivalent elastic modulus values. The predicted time histories of the five elastic parameters are presented in Fig. 14(a)–(e).

To capture the functional dependence between temperature and equivalent stiffness, the second regression model \mathcal{M}_2 is trained to map 24-h lagged temperature data to the corresponding stiffness parameters:

$$\mathbf{E}_b \approx \mathcal{M}_2(\mathbf{T}_b) \quad (24)$$

where \mathbf{T}_b denotes the baseline temperature matrix augmented with 24 lagged intervals to account for thermal inertia effects. The architecture of \mathcal{M}_2 is summarized in Table 6.

The architecture of \mathcal{M}_2 was chosen to reflect the higher input dimensionality of this second regression problem. In contrast to \mathcal{M}_1 , the input now consists of 24 lagged temperature values, introduced to account for thermal inertia effects. Two dropout layers with rate 0.2 were included in the first part of the network to provide stronger regularization than in the inverse surrogate model, since the experimental temperature input is noisier and potentially more correlated than the synthetic modal frequency inputs used for training \mathcal{M}_1 . The subsequent reduction from 256 to 32 neurons was selected to progressively compress the lagged temperature representation toward the 5 effective stiffness parameters. As in the previous model, ReLU activations, standardization of inputs and outputs, and the Adam optimizer with MSE loss were adopted because they provided stable convergence and accurate performance.

The trained model \mathcal{M}_2 is validated using the 20% testing dataset (800 samples). The comparison between actual and predicted stiffness parameters is shown in Fig. 15. Blue lines correspond to actual values, while red lines represent predictions. The MAPE values for each elastic modulus are summarized in Table 7, all remaining below 0.3%, demonstrating high predictive capability.

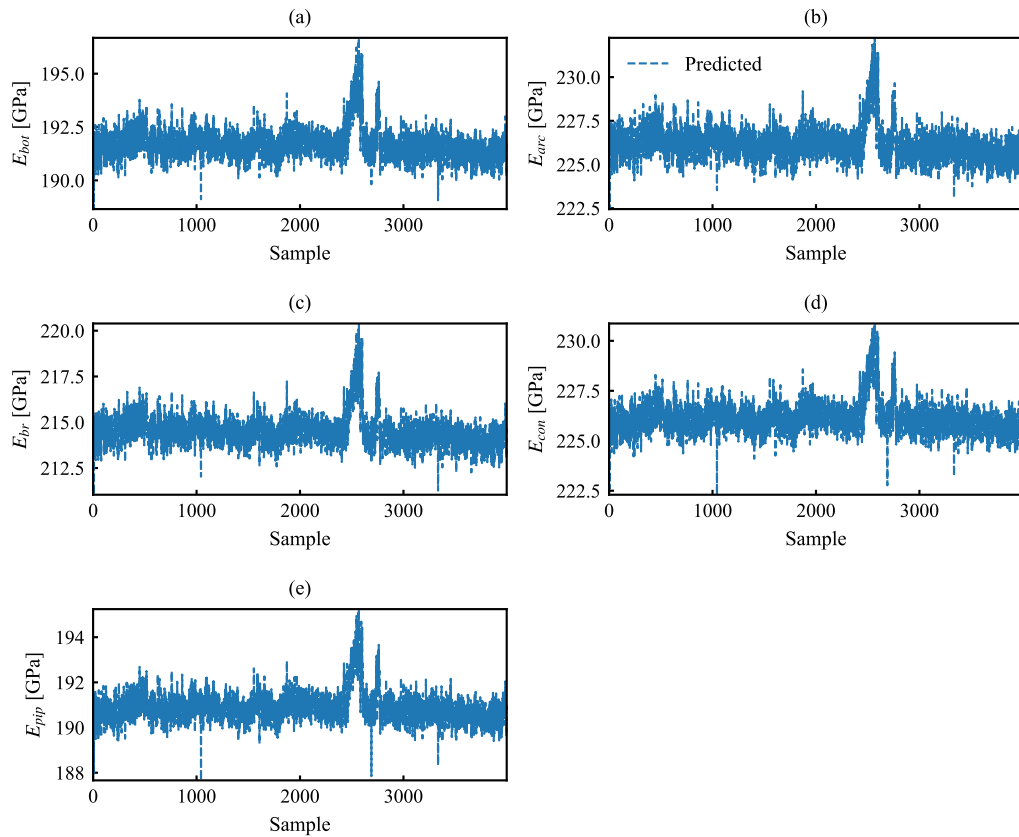


Fig. 14. Predicted evolution of effective Young's moduli from experimental modal frequencies using the inverse surrogate model \mathcal{M}_1 : (a) E_{bot} , (b) E_{arc} , (c) E_{br} , (d) E_{con} , and (e) E_{pip} .

Table 6

Architecture and training configuration of the temperature-to-stiffness regression model \mathcal{M}_2 .

Component	Details
Model type	Deep Neural Network (regression)
Training/Test split	80%/20% (3200/800 samples)
Input layer	24 neurons (lagged temperature inputs)
Hidden layer 1	Dense(256), ReLU activation
Dropout layer 1	Dropout(0.2)
Hidden layer 2	Dense(128), ReLU activation
Dropout layer 2	Dropout(0.2)
Hidden layer 3	Dense(64), ReLU activation
Hidden layer 4	Dense(32), ReLU activation
Output layer	Dense(5)
Loss function	Mean Squared Error (MSE)
Optimizer	Adam (LR = 0.001)
Epochs/Batch size	1000/256
Standardization	Applied to both inputs and outputs

Table 7

Mean Absolute Percentage Error (MAPE) of the temperature-to-stiffness model \mathcal{M}_2 evaluated on the 20% testing dataset.

Parameter	E_{bot}	E_{arc}	E_{br}	E_{con}	E_{pip}
MAPE [%]	0.2510	0.2888	0.2654	0.2270	0.2213

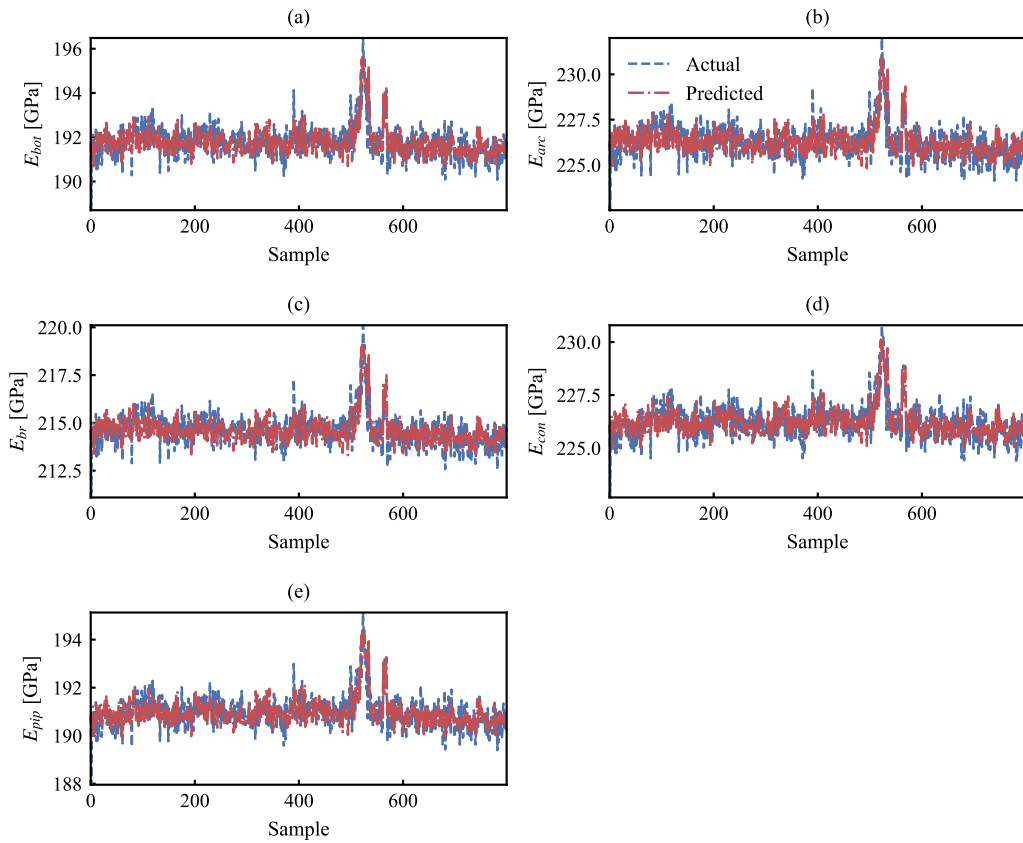


Fig. 15. Comparison of true (blue) and predicted (red) equivalent stiffness parameters for the 20% testing dataset using the temperature-to-stiffness model \mathcal{M}_2 : (a) E_{bot} , (b) E_{arc} , (c) E_{br} , (d) E_{con} , and (e) E_{pip} .

Table 8

Mean Absolute Percentage Error (MAPE) between experimental and predicted modal frequencies for the 800 unseen testing samples.

Mode	f_1	f_2	f_3	f_4	f_5	f_6
MAPE [%]	0.1512	0.1346	0.3346	0.1281	0.4224	0.1827

Step 5 – Verification

To verify the performance of the proposed data-informed temperature modeling strategy, the 800 test samples of Young's moduli (\mathbf{E}_b) obtained from \mathcal{M}_2 , are used as input parameters for the updated FEM and for each of these unseen samples, the corresponding modal frequencies are computed:

$$\hat{\mathbf{F}}_b = \text{FEM}(\mathbf{E}_b). \quad (25)$$

To ensure comparability, the numerically predicted frequencies $\hat{\mathbf{F}}_b$ are aligned with the experimental ones following the same normalization procedure described in Step 4. The aligned frequencies are then compared directly with the experimental modal data \mathbf{F}_{Exp} to evaluate the accuracy of the complete data-informed pipeline.

Fig. 16 presents the comparison between the predicted and experimental modal frequencies for the first 6 modes. Blue lines correspond to the measured frequencies, while red lines denote the predicted ones derived from the temperature data through \mathcal{M}_2 and FEM.

The MAPE values between the predicted and experimental modal frequencies are summarized in Table 8. All 6 MAPE values remain below 0.45%, confirming the model's capability to reproduce realistic temperature-dependent modal variations for the KW51 bridge. It can be observed in some of the modal frequencies (e.g., f_3 and f_5) that the predicted values are smoother and do not reach the largest and smallest values seen in the measurements. This is likely because some of the measured extremes are influenced by noise, while the regularized DNN was trained to capture the physical temperature-dependent trend rather than overfit the noise.

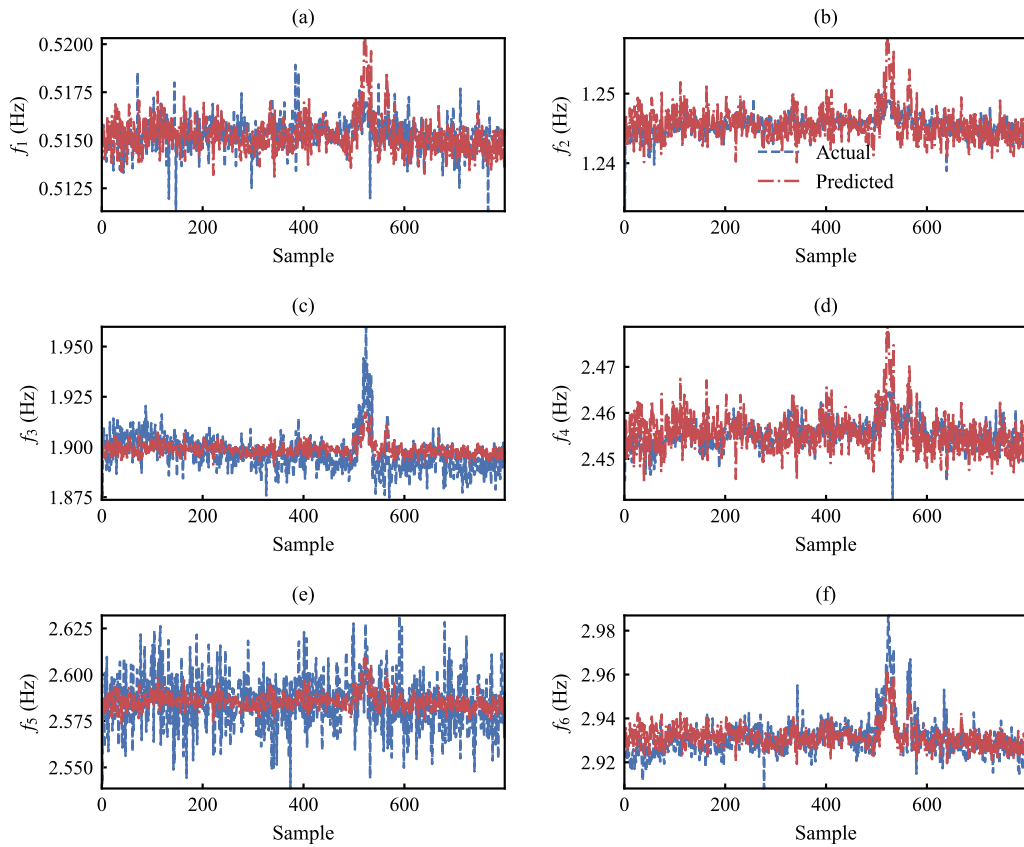


Fig. 16. Comparison between experimental (blue) and predicted (red) modal frequencies obtained from temperature-driven stiffness parameters estimated by \mathcal{M}_2 : (a) f_1 , (b) f_2 , (c) f_3 , (d) f_4 , (e) f_5 , and (f) f_6 .

4.3. Anomaly detection

A central motivation for the proposed framework is to generate synthetic data that remain useful for anomaly detection under realistic environmental variability. In this section, we assess whether the data-informed model, trained on the pre-retrofit baseline, can be transferred to the post-retrofit structural state while preserving the detection behavior observed in the experimental data. To this end, we first evaluate whether the framework reproduces the measured post-retrofit modal frequency evolution using only the lagged post-retrofit temperature history as input. We then investigate whether the post-retrofit state can be detected by the MD-based damage index with respect to the pre-retrofit healthy experimental baseline, and whether the same detection behavior is reproduced by the data-informed model.

Post-retrofit modal frequency prediction. The post-retrofit temperature history, recorded after completion of the strengthening intervention on September 27, 2019, is first provided as input to the trained temperature-to-parameter model. For each time step, the regression model predicts the corresponding effective Young's modulus values of the temperature-sensitive material groups. In addition, the retrofit intervention is introduced explicitly in the numerical model by a 15% increase in the cross-sectional area of the brace-to-deck and brace-to-arch connection elements [15].

Within this simplified numerical representation, the resulting changes in the modal properties are captured most clearly in Modes 2 and 4. For this reason, the post-retrofit comparison is performed using Modes 2 and 4, which provide the most stable and informative indicators of the modeled structural change.

Next, through the Python API of SAP2000 and for each time step, the predicted Young's modulus values and the retrofit effects are applied to the numerical model, after which the eigenvalue problem is solved and the modal frequencies 2 and 4 are extracted. The procedure is repeated for 2500 post-retrofit samples between September 27, 2019 and January 9, 2020.

The resulting frequency trends constitute the *data-informed post-retrofit prediction*, which are compared with the *experimental post-retrofit modal frequencies*, taken here as the ground truth. To ensure consistency between the experimental and numerical domains, the same mean alignment procedure adopted during the construction of the inverse surrogate model is retained here. Specifically, the experimental modal frequencies are shifted according to the difference between the mean values of the pre-retrofit experimental baseline and those obtained from the initial Monte Carlo simulations of the finite element model.

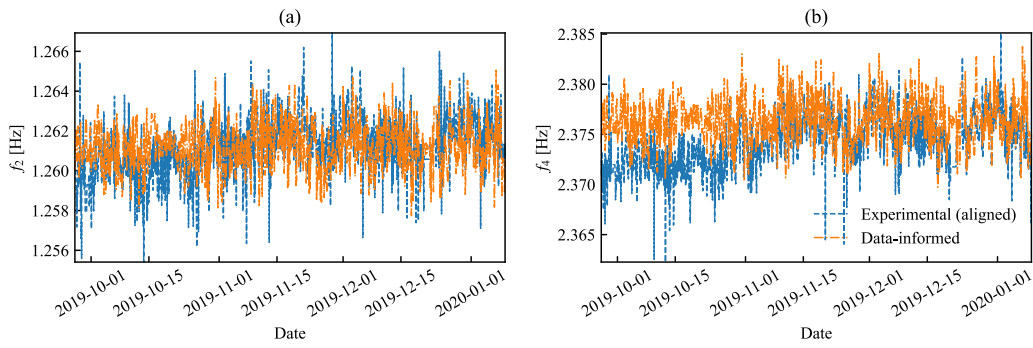


Fig. 17. Comparison between the aligned experimental (blue line) post-retrofit modal frequencies and the data-informed (orange line) predictions for (a) Mode 2 and (b) Mode 4.

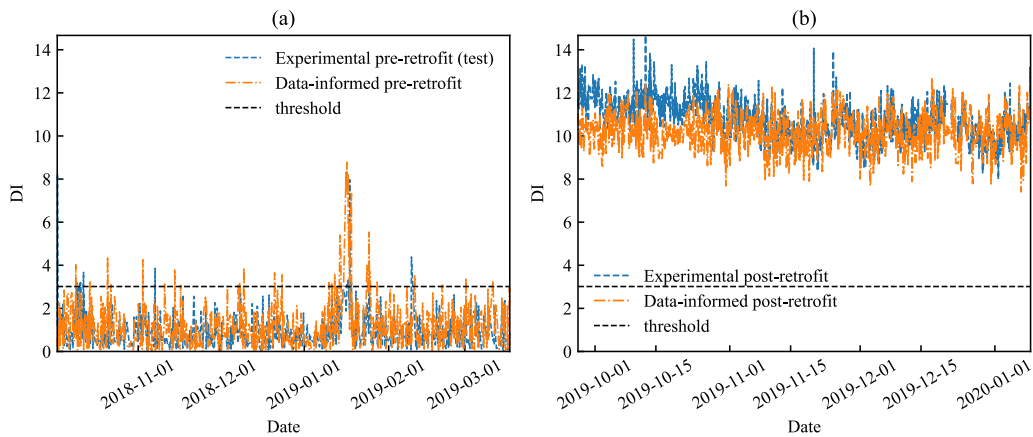


Fig. 18. DIs using modal frequencies 2 and 4 with respect to the pre-retrofit experimental baseline. (a) Testing pre-retrofit data: aligned experimental and data-informed pre-retrofit samples evaluated against the 3200-sample baseline. (b) Post-retrofit data: aligned experimental and data-informed post-retrofit samples evaluated against the same baseline.

For modes 2 and 4, Fig. 17(a) and (b), respectively, show the aligned experimental post-retrofit frequencies (blue) and the corresponding data-informed predictions (orange) as a function of time. A close agreement is obtained, with MAPE values of 0.096% for Mode 2 and 0.125% for Mode 4.

MD-based anomaly detection. The MD damage index is used to evaluate whether the post-retrofit state can be detected with respect to the pre-retrofit condition. Here, the baseline statistics are constructed from the experimental pre-retrofit data used previously for training the temperature-to-parameter regression model.

More specifically, the 3200 pre-retrofit experimental samples used for training are adopted as the pre-retrofit baseline dataset. The remaining 800 experimental pre-retrofit samples are treated as an independent testing dataset. To ensure consistency between the experimental and numerical domains, the same mean-alignment procedure described earlier is applied to all experimental modal frequencies before computing the Mahalanobis distance. To summarize, five datasets are considered:

1. the 3200 pre-retrofit experimental samples used for training, which form the baseline;
2. the 800 experimental pre-retrofit samples used as the testing dataset;
3. the corresponding 800 data-informed pre-retrofit samples generated by the proposed framework;
4. the 2500 experimental post-retrofit samples obtained from monitoring data;
5. the 2500 data-informed post-retrofit samples predicted by the proposed framework using the post-retrofit temperature history.

The MD threshold is defined as the 98th percentile of the baseline pre-retrofit dataset, using only Modes 2 and 4. The resulting threshold is $\tau = 3.014$. Within this detection framework, the two pre-retrofit testing datasets (experimental and data-informed) are used to quantify the PFA, while the experimental and data-informed post-retrofit datasets are used to quantify the POD.

Fig. 18 presents the corresponding DI time histories. Subplot (a) shows the pre-retrofit testing DIs (items 2 and 3), while Subplot (b) shows the post-retrofit phase (items 4 and 5). In both subplots, the horizontal line denotes τ .

Table 9
Anomaly detection results for the KW51 bridge.

Quantity	Experimental	Data-informed
PFA, pre-retrofit testing [%]	1.88	5.88
POD, post-retrofit [%]	100.00	100.00
Mean DI, pre-retrofit testing	0.945	1.211
Std. DI, pre-retrofit testing	0.772	1.129
Mean DI, post-retrofit	10.743	10.181
Std. DI, post-retrofit	0.895	0.817
Threshold τ (98th percentile)	3.014	

The results are summarized in Table 9. For the pre-retrofit testing data, the PFA is 1.88% for the experimental and 5.88% for the data-informed sets. These values remain low in absolute terms, confirming that the proposed framework does not introduce excessive false positives when evaluated against the healthy pre-retrofit baseline.

For the post-retrofit data, both the experimental and the data-informed datasets yield a POD of 100%, indicating that the retrofit-induced shift in modal behavior is consistently detected in both cases. In this case, the mean damage index increases from approximately 0.95–1.21 in the pre-retrofit testing datasets to approximately 10.18–10.74 in the post-retrofit datasets. Moreover, the post-retrofit experimental and data-informed datasets exhibit very similar statistical characteristics, with closely matching mean and standard deviation values.

5. Conclusions

This paper presented a data-informed framework for simulating temperature effects in finite element models for structural health monitoring, with the objective of generating realistic modal datasets for both healthy and damaged structural states. The proposed approach combines monitoring data with an updated FEM through two successive surrogate models: an inverse surrogate that estimates temperature-sensitive parameters of the FEM model from measured modal frequencies, and a second regression model that maps measured temperature to these parameters. In this way, the framework embeds measured thermal effects into the FEM without requiring explicit thermo-mechanical field modeling. The numerical truss example demonstrated the capability of the method under controlled conditions. In addition to reproducing the temperature effect on frequencies, with MAPE values below 1.4% for the first 6 modes, the study also demonstrates the reliability of the proposed approach in generating synthetic frequencies for damage scenarios. Specifically, the analyses conducted using the Mahalanobis distance and PFA/POD metrics as indicators showed that the proposed framework preserves the temperature-driven modal trends of the reference thermo-mechanical model also in unseen damage scenarios.

The experimental application to the KW51 railway bridge confirmed the practical potential of the method on real monitoring data. Using only a single structural thermocouple and lagged temperature inputs, the framework reproduced the measured pre-retrofit modal-frequency evolution with errors below 0.45% for the first 6 modes. An important step in this application was the bias alignment between experimental and numerical modal frequencies, introduced to compensate for the residual mean offset between the updated FEM and the monitored structure. This alignment made the numerical and experimental domains comparable, allowing the inverse surrogate model to be transferred consistently to the measured data while preserving the temperature-dependent variability.

Next, the experimental study considered the post-retrofit condition of the bridge. The post-retrofit temperature history was provided to the trained temperature-to-parameter model, the retrofit intervention was explicitly introduced into the updated FEM, and unseen post-retrofit synthetic frequencies were generated through repeated SAP2000 analyses. The comparison with the measured post-retrofit frequencies showed excellent agreement for the two most informative modes, while the anomaly detection analysis confirmed that both the experimental and data-informed post-retrofit datasets were clearly distinguishable from the pre-retrofit baseline. This result is important because it demonstrates that the proposed framework can be transferred not only to unseen temperature histories, but also to a modified structural state, while still reproducing the corresponding detection behavior in an SHM context.

Overall, the study shows that the proposed framework does more than reproduce average modal-frequency trends. It provides a practical way to generate synthetic temperature-aware data that preserve the detectability characteristics of the reference structural model under environmental variability. This is particularly relevant for SHM applications, where the lack of real damaged data often limits the validation of damage detection strategies and the estimation of reliable thresholds, PFAs, and PODs.

Beyond prediction accuracy, the framework provides several engineering insights relevant to SHM practice. In the numerical example, the analysis reveals that diagonal and bottom-chord damage are more detectable at low severities than top-chord damage, reflecting the stronger contribution of these element groups to the monitored modal frequencies. The framework also enables the estimation of minimum detectable damage under realistic temperature conditions, a metric that cannot be obtained without temperature-aware synthetic data. In the KW51 bridge application, the data-informed model successfully captures the bilinear frequency-temperature behavior observed around 0 °C, which is attributed to frost-induced ballast stiffening and was not explicitly modeled. These results show that the framework can learn non-trivial thermal phenomena directly from the monitoring data and embed them into the FEM simulation.

The framework also has limitations that should be acknowledged. First, the current formulation relies solely on modal frequencies as input to the inverse surrogate. While frequencies are robust and practically available in long-term monitoring, they provide limited spatial information, and extension to other dynamic indicators such as mode shapes or damping ratios could improve parameter identifiability in future applications. Second, the inverse mapping is inherently non-unique, since different parameter combinations may produce similar modal responses. This is mitigated by selecting a reduced set of sensitive parameters, but cannot be fully eliminated. Third, the applicability of the framework to other structural types (e.g., concrete, masonry, or cable-stayed bridges) would depend on the availability of a calibrated FEM and on the sensitivity of the monitored modes to the temperature-sensitive parameters of interest.

Finally, the present framework assumes a stationary healthy baseline, as is common in many SHM applications. Extension to non-stationary conditions, such as progressive deterioration or evolving boundary conditions, would require further development, for instance through adaptive or time-varying regression models.

CRedit authorship contribution statement

Soroosh Kamali: Writing – review & editing, Writing – original draft, Visualization, Validation, Software, Methodology, Investigation, Formal analysis, Data curation, Conceptualization. **Rosario Ceravolo:** Writing – review & editing, Validation, Supervision, Methodology. **Alessandro Marzani:** Writing – review & editing, Validation, Supervision, Resources, Project administration, Methodology, Funding acquisition, Conceptualization.

Acknowledgments

This study was carried out within the “Quantifying the effects of Structure-Soil-Structure interaction on structural modal parameters by combining Earth observation data with on-site dynamic monitoring: an enhanced vibration-based Structural Health Monitoring approach - SAT4SHM” project - funded by European Union - Next Generation EU within the PRIN 2022 PNRR program (D.D.1409 del 14/09/2022 Ministero dell’Università e della Ricerca). This manuscript reflects only the authors’ views and opinions and the Ministry cannot be considered responsible for them.

Declaration of competing interest

The authors declare that they have no known competing financial interests or personal relationships that could have appeared to influence the work reported in this paper.

Appendix A. FEM development and model updating of the KW51 bridge

A detailed finite element model (FEM) of the KW51 railway bridge was developed in SAP2000 to represent the structural configuration before retrofitting, as shown in Fig. A.1, detailed as follows:

Boundary conditions. All four supports allow rotational degrees of freedom. Supports 1 and 3 are fixed in all translational directions, while supports 2 and 4 are constrained only in the vertical (z) and transverse (y) directions, allowing translation along the bridge axis (x).

Structural components. The orthotropic steel deck is modeled using two longitudinal main girders connected by transverse beams and reinforced with longitudinal stiffeners. A 15 mm thick steel plate covers the deck and supports a 0.6 m ballast layer. The deck is suspended from the two main arches by diagonal braces, and connection elements are modeled at each intersection between braces, the arch, and the deck. Four transverse pipe sections tie the two arches together to ensure lateral stability.

Material properties. Steel components are assigned a Young’s modulus of 210 GPa, while the ballast layer is modeled as an elastic medium with a Young’s modulus of 550 MPa.

Section properties. Table A.1 summarizes the geometric and material characteristics of each structural member type, including their shapes, dimensions, and orientations. Colors used in the table correspond to those indicated in Fig. A.1 for visual reference.

Sensitivity analysis. Before performing model updating, a sensitivity analysis was conducted to identify the most influential parameters affecting the dynamic characteristics of the bridge. This analysis was implemented in PYTHON through the Open Application Programming Interface (OAPI), which enables bidirectional communication with the SAP2000 model. A total of 21 candidate parameters were considered, representing both material and geometric properties of the main structural components, as summarized in Table A.2.

The goal of the sensitivity study is to quantify the influence of each parameter on the modal frequencies of the bridge and to identify those with dominant contributions to the dynamic response. Let $f_j(\mathbf{p})$ denote the j th modal frequency as a function of the parameter vector $\mathbf{p} = [p_1, p_2, \dots, p_n]$. The local normalized sensitivity of the j th modal frequency with respect to the i th parameter is expressed as:

$$S_{ij} = \frac{p_i}{f_j} \frac{\partial f_j}{\partial p_i} \quad (\text{A.1})$$

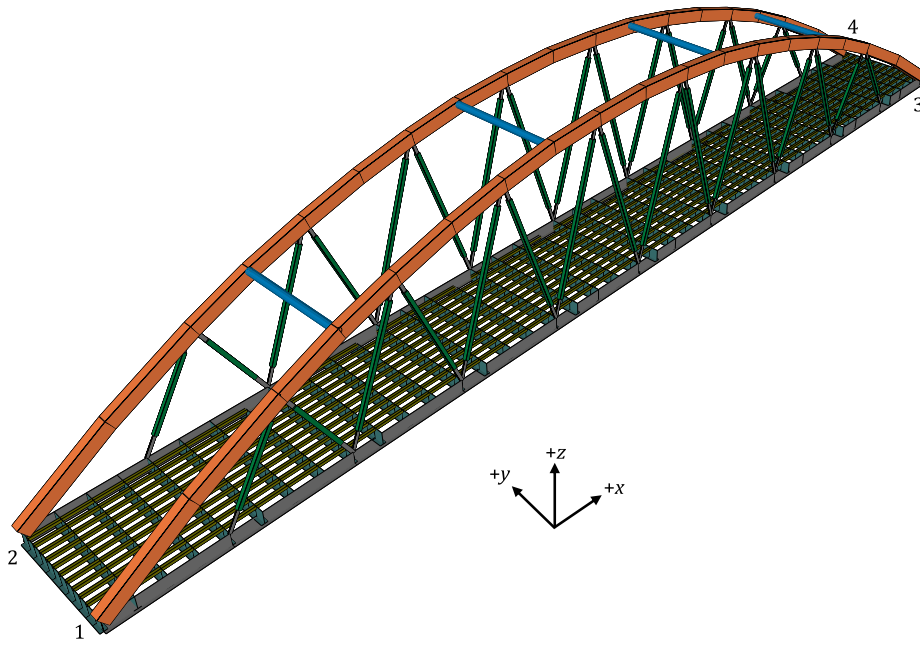


Fig. A.1. Finite element model of the KW51 bridge developed in SAP2000 representing the pre-retrofitting condition.

Table A.1

Section properties and orientations of the FEM of the KW51 bridge, along with corresponding colors used in Fig. A.1. Dimensions are in millimeters.

Section name	Shape	Dimensions	Orientation	Color
e Arch	Box	$1300d \times 860w \times 50t$	yz plane	Orange
Connection	Rectangular	$310d \times 45w$	yz plane	Grey
Girders	Tee	$1235s \times 600f \times 80t$	yz plane	Dark Grey
Deck longitudinal stiffeners	Channel	$250d \times 250w \times 8t$	yz plane	Light Green
Diagonal braces	Box	$350d \times 350w \times 16t$	yz plane	Dark Green
Transverse pipes	Pipe	$750D \times 40t$	xz plane	Blue
Deck transverse beams	Tee	$1235s \times 600f \times 80t$	xz plane	Dark Blue

d = depth, w = width, t = thickness, s = stem, f = flange, D = diameter.

This derivative is approximated numerically using a central finite-difference scheme:

$$S_{ij} \approx \frac{1}{2f_j} \frac{f_j^+ - f_j^-}{(\Delta p_i / p_i)} \quad (\text{A.2})$$

where $\Delta p_i = \epsilon p_i$ is a small perturbation applied to parameter p_i , and $\epsilon = 0.01$ represents a 1% variation. The perturbed frequencies f_j^+ and f_j^- correspond to the results of the FEM when the parameter is increased and decreased by Δp_i , respectively:

$$f_j^+ = f_j(p_1, \dots, p_i + \Delta p_i, \dots, p_n), \quad f_j^- = f_j(p_1, \dots, p_i - \Delta p_i, \dots, p_n)$$

Each sensitivity coefficient S_{ij} therefore quantifies the relative change in modal frequency f_j due to a small normalized variation of parameter p_i . The resulting sensitivity matrix serves to identify the subset of parameters with the strongest dynamic influence, which are subsequently retained for FEM updating.

The normalized local sensitivities S_{ij} were computed for the first 6 identified modal frequencies using the procedure described above. The resulting sensitivity matrix is illustrated as a 3D bar chart (Fig. A.2) and numerically summarized in Table A.3. Positive coefficients indicate parameters whose increase causes a rise in the corresponding modal frequency (e.g., elasticity moduli), whereas negative coefficients imply an inverse relationship, such as mass-related parameters (M_a , M_g) having inverse effect on frequency.

To determine which parameters to retain for model updating, a normalized sensitivity threshold of $|S_{ij}| > 0.1$ was applied. 11 parameters satisfied this criterion and were therefore selected as design variables for the subsequent model calibration: E_{bot} , E_{arc} , E_{br} , E_{con} , E_{pip} , A_c , I_{22p} , A_d , I_{22a} , A_a , and M_a .

Finite element model updating. Having the 11 most influential parameters as design variables, a PYTHON script was developed to communicate with SAP2000 through the OAPI, automating the iterative optimization process. Each parameter acted as a *property modifier* multiplying its nominal value in the finite element model.

Table A.2
Candidate parameters considered for the sensitivity analysis of the KW51 bridge model.

No.	Symbol	Element	Mechanical characteristic
1	E_{bot}	Steel bottom elements	Young's modulus E
2	E_{arc}	Steel arch elements	Young's modulus E
3	E_{br}	Steel brace elements	Young's modulus E
4	E_{con}	Steel connection elements	Young's modulus E
5	E_{pip}	Steel transverse pipes	Young's modulus E
6	E_b	Ballast	Young's modulus E
7	A_c	Connection	Cross-sectional area A
8	A_p	Transverse pipes	Cross-sectional area A
9	I_{33p}	Transverse pipes	Strong moment of inertia I_{33}
10	I_{22p}	Transverse pipes	Weak moment of inertia I_{22}
11	A_d	Diagonal braces	Cross-sectional area A
12	I_{33a}	Arch	Strong moment of inertia I_{33}
13	I_{22a}	Arch	Weak moment of inertia I_{22}
14	A_a	Arch	Cross-sectional area A
15	J_a	Arch	Torsional constant J
16	M_a	Arch	Mass M
17	I_{33g}	Deck T-beam girders	Strong moment of inertia I_{33}
18	I_{22g}	Deck T-beam girders	Weak moment of inertia I_{22}
19	M_g	Deck T-beam girders	Mass M
20	A_{tb}	Deck transverse T-beams	Cross-sectional area A
21	I_{22s}	Deck U-stiffeners	Weak moment of inertia I_{22}

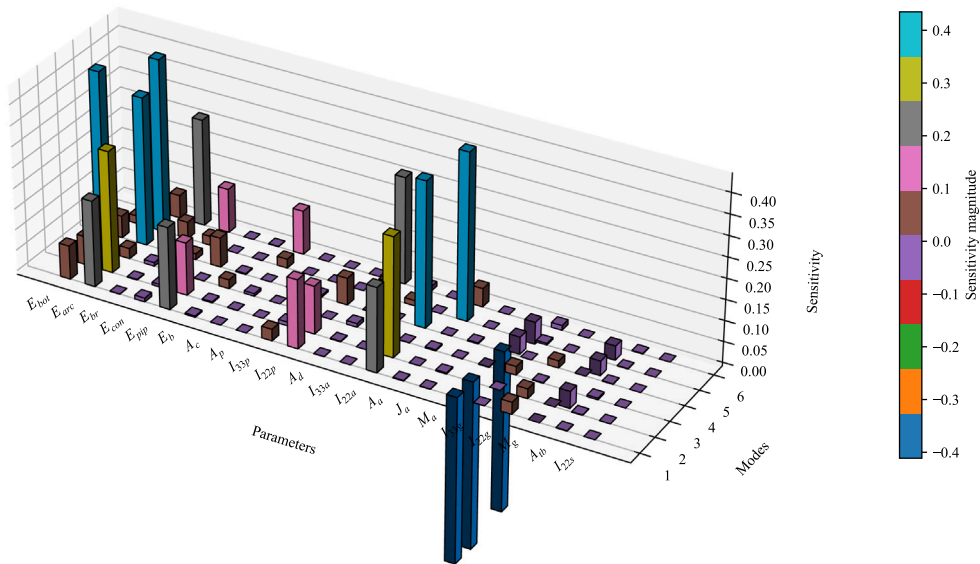


Fig. A.2. Normalized local sensitivities of the first 6 modal frequencies with respect to the 21 candidate parameters of the KW51 bridge model.

The optimization problem aimed to minimize the discrepancy between the experimental modal frequencies (identified from pre-retrofitting monitoring data) and the numerical frequencies obtained from the FEM. The objective function was defined as:

$$z = \sum_{j=1}^6 \left(\frac{f_j^{Num} - f_j^{Exp}}{f_j^{Exp}} \right)^2 \tag{A.3}$$

where f_j^{Exp} and f_j^{Num} denote, respectively, the experimental and numerical natural frequencies for the j th mode.

For the optimization task, the bounds were set to $\pm 10\%$ for the elastic moduli (E_s) and $\pm 50\%$ for all other parameters. The model updating was carried out using the Limited-memory Broyden–Fletcher–Goldfarb–Shanno (L-BFGS) algorithm [46] implemented in the SciPy optimization library [47]. A maximum of 20 iterations was specified as the convergence criterion. Upon convergence, the algorithm provided the optimal scaling factors listed in Table A.4, which were applied as multiplicative modifiers to the initial FEM parameters. Finally, Table A.5 compares the experimental, un-updated, and updated FEM results for the first 6 vibration modes.

The results demonstrate that the updating process effectively reduced the average frequency error from approximately 6.9% to below 1%. The updated FEM was subsequently employed as the reference numerical model for the temperature-frequency relationship analysis described in the KW51 bridge case study.

Table A.3

Normalized sensitivities of the first 6 modal frequencies with respect to the 21 candidate parameters. Cells shaded in light gray indicate $|S_{ij}| > 0.1$.

Parameter	$S(f_1)$	$S(f_2)$	$S(f_3)$	$S(f_4)$	$S(f_5)$	$S(f_6)$
E_{bot}	0.0810	0.0686	0.4350	0.0531	0.0191	0.0784
E_{arc}	0.2076	0.2936	0.0251	0.3582	0.4184	0.0557
E_{br}	0.0007	0.0019	0.0088	0.0011	0.0403	0.2584
E_{con}	0.0092	0.0060	0.0093	0.0142	0.0219	0.1065
E_{pip}	0.1982	0.1271	0.0004	0.0711	0.0000	0.0000
E_b	0.0033	0.0028	0.0215	0.0023	0.0004	0.0011
A_c	0.0003	0.0007	0.0062	0.0003	0.0218	0.1057
A_p	0.0000	0.0000	0.0000	0.0000	0.0000	0.0000
I_{33p}	0.0281	0.0088	0.0001	0.0046	0.0000	0.0000
I_{22p}	0.1653	0.1152	0.0001	0.0648	0.0000	0.0000
A_d	0.0006	0.0017	0.0086	0.0005	0.0403	0.2581
I_{33a}	0.0002	0.0002	0.0205	0.0001	0.0129	0.0107
I_{22a}	0.2031	0.2875	0.0008	0.3509	0.0000	0.0000
A_a	0.0016	0.0004	0.0029	0.0004	0.4029	0.0447
J_a	0.0007	0.0027	0.0004	0.0027	0.0000	0.0000
M_a	-0.4081	-0.4113	-0.0011	-0.3963	-0.0420	-0.0533
I_{33g}	0.0002	0.0002	0.0206	0.0001	0.0040	0.0115
I_{22g}	0.0285	0.0234	0.0014	0.0173	0.0000	0.0001
M_g	0.0000	0.0000	-0.0407	-0.0001	-0.0355	-0.0343
A_{tb}	0.0013	0.0012	0.0040	0.0011	0.0012	0.0014
I_{22s}	0.0002	0.0002	0.0001	0.0001	0.0000	0.0001

Table A.4

Optimized property modifiers for the 11 design variables after FEM updating. Each modifier is multiplied by the nominal parameter value in the original model.

Parameter	Optimized multiplier
E_{bot}	0.9324
E_{arc}	1.1000
E_{br}	1.0432
E_{con}	1.1000
E_{pip}	0.9286
A_c	1.2188
I_{22p}	0.6416
A_d	1.4826
I_{22a}	1.5000
A_a	1.0540
M_a	0.9710

Table A.5

Comparison of experimental, un-updated, and updated FEM modal frequencies for the KW51 bridge.

Mode number	Experimental	FEM (Un-updated)		FEM (Updated)	
	f [Hz]	f [Hz]	Error [%]	f [Hz]	Error [%]
1	0.51	0.4735	7.16	0.5040	1.17
2	1.24	1.1080	10.65	1.2754	2.86
3	1.89	1.7190	9.05	1.8885	0.08
4	2.45	2.3450	4.29	2.4033	1.91
5	2.58	2.4870	3.60	2.5797	0.01
6	2.92	2.7810	4.76	2.9202	0.01

Data availability

The data, finite element model, and API codes will be made available on request.

References

- [1] Y. Bao, H. Li, Machine learning paradigm for structural health monitoring, *Struct. Health Monit.* 20 (4) (2021) 1353–1372.
- [2] C.R. Farrar, K. Worden, *Structural Health Monitoring: a Machine Learning Perspective*, John Wiley & Sons, 2012.
- [3] Y.-J. Cha, R. Ali, J. Lewis, O. Büyüköztürk, Deep learning-based structural health monitoring, *Autom. Constr.* 161 (2024) 105328.

- [4] S. Kamali, S. Quqa, A. Palermo, A. Marzani, Reducing false alarms in structural health monitoring systems by exploiting time information via binomial distribution classifier, *Mech. Syst. Signal Process.* 207 (2024) 110938.
- [5] S. Coccimiglio, G. Miraglia, V. Cavanni, A. Crocetti, R. Ceravolo, Automated mode tracking via supervised classification and adaptive parameter calibration for seismic monitoring with sparse sensors, *Bull. Earthq. Eng.* (2025) 1–27.
- [6] F.M. Bono, A. Argentino, L. Bernardini, L. Benedetti, G. Cazzulani, C. Somaschini, M. Belloli, Automated operational modal analysis of a steel truss railway bridge employing free decay response, *J. Infrastruct. Intell. Resil.* 4 (1) (2025) 100145.
- [7] O. Markogiannaki, A. Arailopoulos, D. Giagopoulos, C. Papadimitriou, Vibration-based damage localization and quantification framework of large-scale truss structures, *Struct. Health Monit.* (2022) 14759217221100443.
- [8] H. Zhou, Y. Ni, J. Ko, Structural damage alarming using auto-associative neural network technique: Exploration of environment-tolerant capacity and setup of alarming threshold, *Mech. Syst. Signal Process.* 25 (5) (2011) 1508–1526.
- [9] E. Figueiredo, J. Brownjohn, Three decades of statistical pattern recognition paradigm for SHM of bridges, *Struct. Health Monit.* 21 (6) (2022) 3018–3054.
- [10] S. Kamali, A. Palermo, A. Marzani, Virtual baseline to improve anomaly detection of SHM systems with non-stationary data, *Mech. Syst. Signal Process.* 224 (2025) 111968.
- [11] S. Coccimiglio, G. Miraglia, R. Ceravolo, Experimental study on the influence of environmental variables on the dynamic monitoring of full-scale structures, in: *International Conference on Experimental Vibration Analysis for Civil Engineering Structures*, Springer, 2025, pp. 155–164.
- [12] A. Argentino, L. Radicioni, F.M. Bono, L. Bernardini, L. Benedetti, G. Cazzulani, C. Somaschini, M. Belloli, Data normalization for the continuous monitoring of a steel truss bridge: A case study from the Italian railway line, *J. Infrastruct. Intell. Resil.* (2025) 100171.
- [13] S. Ereiz, I. Duvnjak, J.F. Jiménez-Alonso, Review of finite element model updating methods for structural applications, in: *Structures*, vol. 41, Elsevier, 2022, pp. 684–723.
- [14] S. Bi, M. Beer, S. Cogan, J. Mottershead, Stochastic model updating with uncertainty quantification: an overview and tutorial, *Mech. Syst. Signal Process.* 204 (2023) 110784.
- [15] S. Kamali, S. Quqa, A. Palermo, A. Marzani, The role of finite element model updating in homogeneous transfer learning for damage classification in structural health monitoring, *Mech. Syst. Signal Process.* 239 (2025) 113298.
- [16] E. Lenticchia, G. Miraglia, J.A.C. Lopez, R. Ceravolo, Sensitivity driven model updating: a multi-step procedure for structural assessment, *J. Build. Eng.* (2025) 112941.
- [17] S. Kamali, A. Marzani, L. Sciuolo, M. Di Felice, G. Augugliaro, C. Mennuti, Temperature compensation in vibration-based structural health monitoring using neural network regression, in: *2023 7th International Conference on System Reliability and Safety, ICSRS, IEEE*, 2023, pp. 36–42.
- [18] C. Liu, J.T. DeWolf, Effect of temperature on modal variability of a curved concrete bridge under ambient loads, *J. Struct. Eng.* 133 (12) (2007) 1742–1751.
- [19] M.A. Wahab, G. De Roeck, Effect of temperature on dynamic system parameters of a highway bridge, *Struct. Eng. Int.* 7 (4) (1997) 266–270.
- [20] Y.L. Xu, B. Chen, C. Ng, K. Wong, W. Chan, Monitoring temperature effect on a long suspension bridge, *Struct. Control. Health Monit.* 17 (6) (2010) 632–653.
- [21] J. Luo, M. Huang, Y. Lei, Temperature effect on vibration properties and vibration-based damage identification of bridge structures: A literature review, *Buildings* 12 (8) (2022).
- [22] R. Kromanis, P. Kripakaran, SHM of bridges: characterising thermal response and detecting anomaly events using a temperature-based measurement interpretation approach, *J. Civ. Struct. Health Monit.* 6 (2) (2016) 237–254.
- [23] Y. Ding, A. Li, Temperature-induced variations of measured modal frequencies of steel box girder for a long-span suspension bridge, *Int. J. Steel Struct.* 11 (2) (2011) 145–155.
- [24] B. Moaveni, I. Behmanesh, Effects of changing ambient temperature on finite element model updating of the dowling hall footbridge, *Eng. Struct.* 43 (2012) 58–68.
- [25] L.M. Sun, W. Zhang, S. Nagarajaiah, Bridge real-time damage identification method using inclination and strain measurements in the presence of temperature variation, *J. Bridg. Eng.* 24 (2) (2019) 04018111.
- [26] Y. Xia, B. Chen, X.-q. Zhou, Y.-l. Xu, Field monitoring and numerical analysis of tsing ma suspension bridge temperature behavior, *Struct. Control. Health Monit.* 20 (4) (2013) 560–575.
- [27] L. Zhou, Y. Xia, J.M. Brownjohn, K.Y. Koo, Temperature analysis of a long-span suspension bridge based on field monitoring and numerical simulation, *J. Bridg. Eng.* 21 (1) (2016) 04015027.
- [28] Y. Zhou, X. Xu, G. Hao, Z. Wei, Y. Liu, F. Yi, Temperature-based structural identification of long-span bridges using InSAR observation and meteorological shared data, *Adv. Struct. Eng.* (2025) 13694332251340715.
- [29] P. Borlenghi, A. Saisi, C. Gentile, Vibration monitoring of masonry bridges to assess damage under changing temperature, *Dev. Built Environ.* 20 (2024) 100555.
- [30] P. Borlenghi, A. Saisi, C. Gentile, Effects of changing temperature in the vibration-based model updating of a masonry bridge, in: *Life-Cycle of Structures and Infrastructure Systems*, CRC Press, 2023, pp. 1552–1559.
- [31] Q. Xia, L. Zhou, J. Zhang, Thermal performance analysis of a long-span suspension bridge with long-term monitoring data, *J. Civ. Struct. Health Monit.* 8 (4) (2018) 543–553.
- [32] P. Salcher, C. Adam, Modelling strategies for the seasonal effects on dynamic bridge parameters, *Mecc. Dei Mater. E Delle Strutt.* VI (2016) 107–114.
- [33] M. van de Velde, D. Anastasopoulos, H. De Backer, E. Reynders, G. Lombaert, Modal strain monitoring of a post-tensioned concrete girder bridge: Influence of temperature and solar irradiation, *Eng. Struct.* 329 (2025) 119832.
- [34] D. Anastasopoulos, K. Maes, G. De Roeck, G. Lombaert, E. Reynders, Structural health monitoring of the KW51 bridge based on detailed strain mode shapes: Environmental influences versus simulated damage, in: *Life-Cycle of Structures and Infrastructure Systems*, CRC Press, 2023, pp. 391–398.
- [35] S. Kamali, S. Mariani, M. Hadianfard, A. Marzani, Inverse surrogate model for deterministic structural model updating based on random forest regression, *Mech. Syst. Signal Process.* 215 (2024) 111416.
- [36] K. Maes, G. Lombaert, Monitoring railway bridge KW51 before, during, and after retrofitting, *J. Bridg. Eng.* 26 (3) (2021) 04721001.
- [37] K. Maes, G. Lombaert, Monitoring data for railway bridge KW51 in Leuven, Belgium, before, during, and after retrofitting, 2020, <http://dx.doi.org/10.5281/zenodo.3745914>.
- [38] M. Seif, L. Choe, J. Gross, W.E. Luecke, J.A. Main, D. McColskey, F. Sadek, J.M. Weigand, C. Zhang, Temperature-Dependent Material Modeling for Structural Steels: Formulation and Application, US Department of Commerce, National Institute of Standards and Technology, 2016.
- [39] D.P. Kingma, J. Ba, Adam: A method for stochastic optimization, 2014, arXiv preprint arXiv:1412.6980.
- [40] S. Kamali, S. Quqa, A. Palermo, A. Marzani, An approach to define the minimum detectable damage and the alarm thresholds in vibration-based shm systems, in: *Journal of Physics: Conference Series*, vol. 2647, (18) IOP Publishing, 2024, 182008.
- [41] B. Peeters, G. De Roeck, Reference-based stochastic subspace identification for output-only modal analysis, *Mech. Syst. Signal Process.* 13 (6) (1999) 855–878.
- [42] S. Kamali, S. Mariani, A. Marzani, Temperature compensation in vibration-based structural health monitoring: Static versus dynamic regression models, in: *Operational Modal Analysis*, CRC Press, 2026, pp. 84–99.
- [43] C. Jiang, Z. Yang, CKNNI: an improved knn-based missing value handling technique, in: *Advanced Intelligent Computing Theories and Applications: 11th International Conference, ICIC 2015, Fuzhou, China, August 20-23, 2015. Proceedings, Part III 11*, Springer, 2015, pp. 441–452.

- [44] K. Maes, L. Van Meerbeeck, E. Reynders, G. Lombaert, Validation of vibration-based structural health monitoring on retrofitted railway bridge KW51, *Mech. Syst. Signal Process.* 165 (2022) 108380.
- [45] R. Brincker, C. Ventura, *Introduction to Operational Modal Analysis*, John Wiley & Sons, 2015.
- [46] D.C. Liu, J. Nocedal, On the limited memory BFGS method for large scale optimization, *Math. Program.* 45 (1) (1989) 503–528.
- [47] P. Virtanen, R. Gommers, T.E. Oliphant, M. Haberland, T. Reddy, D. Cournapeau, E. Burovski, P. Peterson, W. Weckesser, J. Bright, et al., SciPy 1.0: fundamental algorithms for scientific computing in python, *Nature Methods* 17 (3) (2020) 261–272.